Retrieval of At-Surface Upwelling Radiance and Albedo by Parameterizing Cloud Scattering and Transmittance over Rugged Terrain

Jia, Junru; Menenti, Massimo; Jia, Li; Chen, Qiting; Xu, Anlun

DOI
10.3390/rs16101723

Publication date
2024

Document Version
Final published version

Published in
Remote Sensing

remote sensing

MDPI

Article

Retrieval of At-Surface Upwelling Radiance and Albedo by Parameterizing Cloud Scattering and Transmittance over Rugged Terrain

Junru Jia [1,2], Massimo Menenti [1,3], Li Jia [1,*], Qiting Chen [1] and Anlun Xu [4]

[1] Key Laboratory of Remote Sensing and Digital Earth, Aerospace Information Research Institute, Chinese Academy of Sciences, Beijing 100101, China; jiajr@radi.ac.cn (J.J.); m.menenti@radi.ac.cn (M.M.); chenqt@aircas.ac.cn (Q.C.)
[2] University of Chinese Academy of Sciences, Beijing 100049, China
[3] Faculty of Civil Engineering and Earth Sciences, Delft University of Technology, 2628 CN Delft, The Netherlands
[4] Dali National Climate Observatory, Dali 671003, China; xualun@126.com
* Correspondence: jiali@aircas.ac.cn; Tel.: +86-10-6480-7982

Abstract: Accurate and continuous estimation of surface albedo is vital for assessing and understanding land–surface–atmosphere interactions. We developed a method for estimating instantaneous all-sky at-surface shortwave upwelling radiance and albedo over the Tibetan Plateau. The method accounts for the complex interplay of topography and atmospheric interactions and aims to mitigate the occurrence of data gaps. Employing an RTLSR-kernel-driven model, we retrieved surface shortwave albedo with a 1 km resolution, incorporating direct, isotropic diffuse; circumsolar diffuse; and surrounding terrain irradiance into the all-sky solar surface irradiance. The at-surface upwelling radiance and surface shortwave albedo estimates were in satisfactory agreement with ground observations at four stations in the Tibetan Plateau, with RMSE values of 56.5 W/m^2 and 0.0422, 67.6 W/m^2 and 0.0545, 98.6 W/m^2 and 0.0992, and 78.0 98.6 W/m^2 and 0.639. This comparison indicated an improved accuracy of at-surface upwelling radiance and surface albedo and significantly reduced data gaps. Valid observations increased substantially in comparison to the MCD43A2 data product, with the new method achieving an increase ranging from 40% to 200% at the four stations. Our study demonstrates that by integrating terrain, cloud properties, and radiative transfer modeling, the accuracy and completeness of retrieved surface albedo and radiance in complex terrains can be effectively improved.

Keywords: land surface albedo; at-surface upwelling radiance; Tibetan Plateau; rugged terrain

Citation: Jia, J.; Menenti, M.; Jia, L.; Chen, Q.; Xu, A. Retrieval of At-Surface Upwelling Radiance and Albedo by Parameterizing Cloud Scattering and Transmittance over Rugged Terrain. *Remote Sens.* **2024**, *16*, 1723. https://doi.org/10.3390/rs16101723

Academic Editor: Yi Luo

Received: 4 March 2024
Revised: 15 April 2024
Accepted: 16 April 2024
Published: 13 May 2024

1. Introduction

The land surface albedo is defined as the proportion of the total incident solar irradiance reflected in the 0.2–5 μm wavelength range in the viewing hemisphere [1–4]. It is a primary factor controlling the land surface radiation balance and significantly influences water and heat balances at the interface of the Earth's surface and the atmosphere. The spatial and temporal variation of land surface albedo introduces perturbations in radiative forcing, which drives land cover conditions, regional to global climate and environmental changes [3]. Accordingly, it is a crucial land surface property in both climate and land surface processes models [5]. The literature documents the accuracy of albedo required for climate modeling, e.g., ±0.05 according to [3] and ±0.02 according to [6]. The Tibetan Plateau is the world's highest plateau and mountain area, with a mean elevation of approximately 4500 m.a.s.l. (meters above sea level). It is the third-largest reservoir of water ice in the world and is often referred to as the Water Tower of Asia. As a high-elevation heat and water source, the energy balance of the Tibetan Plateau significantly influences

both regional and global weather and climate [7]. Investigating the spatial and temporal variations of land surface albedo and better understanding the intricate climate–surface albedo feedbacks in the Tibetan Plateau is of great importance in the context of regional and global climate [8].

(a) Current approaches to retrieving land surface albedo and limitations due to cloud cover

Currently, satellite data offer a practical technique to estimate albedo at larger scales, and numerous algorithms and products on surface albedo have been developed over several decades. Since the launch of the Terra (1999) and Aqua (2002) satellites carrying the Moderate Resolution Imaging Spectroradiometer (MODIS), the estimation of land–surface albedo using remote sensing data has advanced significantly [9]. The MODIS retrieval system of the MCD43 product generates multiple BRDF data products [10]. The most accurate and reliable retrieval description of the BRDF is obtained by fitting the Ross Thick-Li Sparse (RTLSR) BRDF model to available cloud-free observations within each 16 day window (referred to as "full model inversion").

The retrieval of land surface albedo from polar-orbiting satellite data includes three main steps: estimation of the at-surface reflectance, modeling of the bidirectional reflectance distribution function (BRDF), and narrow-to-broadband conversion of albedo [9,11]. MCD43A Version 6 (V006.1) is the newest daily MODIS surface albedo product. The MODIS albedo algorithm uses cloudless atmospherically corrected bidirectional reflectance data (BRF, i.e., the MODIS level-2 surface reflectance product) as input and takes into account the quality flag to select observations in the spectral bands 1 through 7 (i.e., from 620 nm to 2155 nm) of MODIS level 1B data, which has been calibrated and geolocated using at-aperture radiances [9] The MODIS surface reflectance product is corrected for the effects of atmospheric gases and aerosol only, i.e., it applies to clear sky conditions over flat terrain.

A semiempirical kernel-driven model, i.e., the RossThick-LiSparseR (RTLSR) kernel-driven BRDF model, is used in the MODIS BRDF/albedo product algorithm to describe the BRDF as a linear combination of three kernels: isotropic scattering, volume scattering, and geometric optics scattering [10]. This requires three kernel-weighting coefficients, which are least-squares estimates using clear-sky at-surface reflectance. At least seven clear-sky observations during a 16-day period are required in the full model inversion, in which a linear RTLSR kernel-driven bidirectional reflectance distribution function (BRDF) model is fitted using least squares to obtain the BRDF parameters [11,12]. The semiempirical kernel-driven model reconstructs the BRDF for any illumination and view geometry. If the results of the full model inversion are unsatisfactory, or if the number of clear-sky observations are insufficient ($4 \leq$ number of observations < 7 in the MODIS Collection V004 and V005 BRDF/albedo product, and $2 \leq$ number of observations < 7 in the MODIS Collection V006 BRDF/albedo product), the magnitude inversion method is used. This magnitude inversion uses the available multi-angle clear-sky observations to adjust the a priori BRDF parameters to update the RTSLR parameters to be consistent with the actual surface conditions [11,12]. If the results of the magnitude inversion are unsatisfactory, or if the number of observations are less than the minimum number of observations required as mentioned above, no retrieval results are available, and the pixel is assigned a value using a global BRDF database.

Despite using 16 days of accumulated surface reflectance data, it is at times not possible to gather the sufficient clear-sky multi-angular observations of surface reflectance to fulfill the minimum requirements of the BRDF model due to cloud coverage [13]. From 2000 to 2009, annually, approximately 20% to 40% of global land pixels lack daily valid retrievals sufficient to meet the requirements of the BRDF model [14]. Particularly in the Tibetan Plateau region, the MODIS albedo product struggles to gather sufficient valid retrievals. Due to cloud cover, atmospheric contamination, sensor malfunction and variations in surface topography, there are many gaps in the land surface albedo data set [9,15].

Cloud cover is the primary factor that impacts the retrieval of albedo, as it limits the number of clear-sky observations. This scarcity of clear-sky multi-angular observations affects the quality of albedo retrieval, sometimes even preventing successful retrieval.

Given the importance of spatial and temporal continuity of the observations required for various applications, algorithms designed for gap-filling are essential to filling in missing data. Enhancing input data quality for surface albedo estimation and filling gaps in existing albedo products are key strategies to improve current albedo datasets [14,16–19].

(b) Terrain effects on irradiance and reflected radiance

Terrain effects have a significant impact on both incoming solar radiance and outgoing reflected radiance, ultimately playing a substantial role in the estimation of surface albedo. Surface albedo changes with the illumination and viewing geometries, particularly in mountain areas, due to the combination of effects at the observed target and on the surrounding terrain. The change in surface albedo with the direct and diffuse irradiance, the evolution of the surface cover type, especially rapid and short-lived changes due to snowfall, and the topographic effect regulating the direct, diffuse and terrain-reflected radiation [20] need to be accounted for in the retrieval of land surface albedo.

Land surface albedo can then be retrieved once the BRDF is established. The semiempirical kernel-driven model is used to describe how reflectance varies with illumination and view angles, which is applied to each spectral channel of the instrument. There has been growing consideration of terrain effects in the remote-sensing-based surface albedo algorithms in recent years. Gao et al. [21] proposed an improved retrieval method by adding a topographic factor to the MODIS Bidirectional Reflectance Anisotropy of Land Surface model. However, this method did not address the correction of land surface reflectance in obstructed pixels in rugged areas and ignored the reflected sky diffuse irradiance. Wen et al. [22] proposed an extended multi-sensor combined BRDF inversion model to characterize subpixel-scale effects, which performed well compared to the ground measurement.

(c) All-sky retrieval of surface albedo

In some studies [23–25], researchers delved deeper into estimating downwelling solar radiation in alpine regions under all sky conditions and worked towards improving the accuracy of retrieved surface albedo. Efficiently and accurately estimating radiation under cloudy skies is crucial due to the substantial influence of cloud cover on the data acquired by optical remote sensors. Previous studies have used numerous satellite-based parameters as inputs for complex radiative transfer models [26,27]. These models incorporate detailed descriptions of physical processes, but they are resource-intensive due to numerous variables and the high computational burden limits the spatial resolution of the outcomes [28]. A possible solution is to use lookup tables generated offline. LUTs are created through the application of atmospheric radiative transfer models across numerous scenarios. These model outputs are then resampled to develop LUTs for downwelling solar radiation estimation. The advantage of LUT-based methods is their avoidance of complex input parameters at the retrieval stage [29]. As regards the treatment of radiative transfer under cloudy conditions, parameterization methods have been established [30–32]. Many parameterization schemes are spectrum-dependent [33,34]. Van Laake and Sanchez-Azofeifa et al. [33] applied the cloud parameterization model of Stephens et al. [30] to estimate photosynthetically active radiation (PAR) using MODIS atmospheric products. Huang et al. [35] used a broadband parameterization to estimate solar surface irradiance (SSI) inspired by the cloud parameterization model of Fu et al. [32].

Modern techniques and methodologies, like those used in the Satellite Application Facility on Climate Monitoring (CM-SAF) all-sky data, effectively simulate cloud reflectance and attenuation effects on radiative flux, despite cloud complex microphysical and optical properties. Several estimation approaches exist, including empirical relationships, physical principles, optimization techniques, and machine learning models [36–41].

(d) Overview of the new approach

Recognizing the limitations of current approaches, especially under all-sky and rugged terrain conditions, this study aims to introduce an innovative method for estimating surface albedo and at-surface upwelling radiance over the Tibetan Plateau using MODIS data. We have been able to estimate the components of surface solar irradiance and of

upwelling radiance: direct, isotropic and circumsolar diffuse, and terrain irradiance over rugged terrain under cloudy sky [42]. The approach proposed in this paper aimed to substantially reduce the occurrence of data gaps and improve the quality of the estimated albedo. Notably, in an earlier study, we focused on the estimation of the surface solar irradiance (SSI) and its four components, i.e., direct, isotropic diffuse, circumsolar diffuse, and surrounding terrain irradiance, factoring in the actual terrain geometry derived from DEM data [42]. Under cloudy conditions, our model integrates cloud properties, such as cloud cover fraction and cloud reflectance and transmittance, to improve the estimation of SSI and at-surface upwelling radiance. This method allows for an estimation of bidirectional surface reflectance even under cloudy conditions, improving the continuity of input data for BRDF modelling and the retrieval of surface albedo. As in the MODIS algorithm, the anisotropy of the bidirectional reflectance of the land surface is described using the RTLSR-kernel-driven BRDF model in our study. The semiempirical kernel-driven model is applied to reconstruct the BRDF, but the reflectances are calculated for the four components of surface solar irradiance under all sky conditions. Ultimately, the surface albedo is calculated as the ratio of the total reflected radiance to the total incident solar irradiance, aligning with the fundamental definition of surface albedo. Our method enables daily albedo estimation in a region critically important for global climate dynamics.

2. Description of Study Area and Data

2.1. Study Area and In Situ Radiation Observations

The Tibetan Plateau is encompassed by formidable mountain ranges: the Inner Himalayas to the south, the Arkin Qilian Mountains to the north, the Karakorum Mountains to the west, and the Hengduan Mountains to the east, as illustrated in Figure 1. This plateau, the largest in China and the highest globally, spans an approximate area of 2.05 million km², accounting for a quarter of China's landmass. The average elevation of the plateau exceeds 4500 m above sea level (m.a.s.l.).

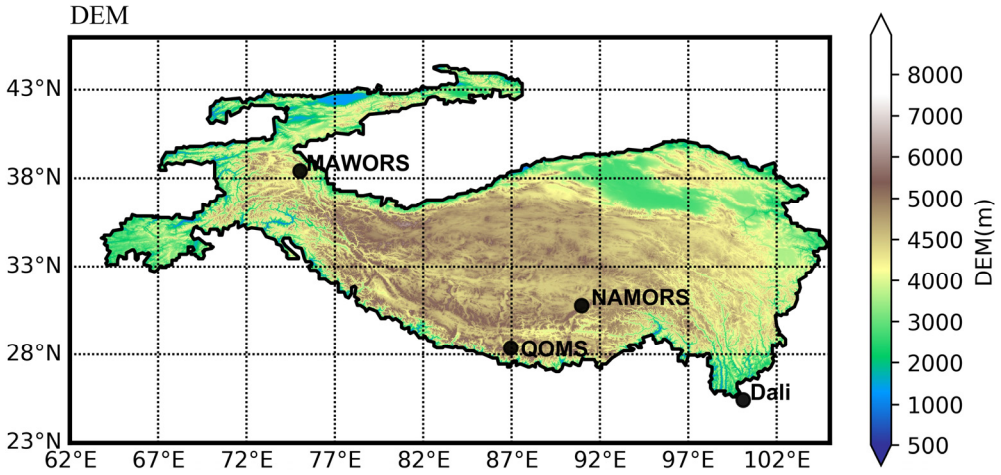

Figure 1. A DEM map of the third pole showing the study area and locations of the ground stations (black dots).

The ground measurements were obtained from radiation balance stations located on the Tibetan Plateau (Table 1 and Figure 1), namely the NamCo Monitoring and Research for Multisphere Interactions Station (NAMORS), the Dali Station, Muztagh Ata for Westerly Environment Observation and Research Station (MWWORS), and Qomolangma Atmospheric and Environmental Observation and Research Station (QOMS). The four stations—with MAWORS in the westerly zone and QOMS, NAMORS, and Dali in the monsoon zone—are geographically and climatically positioned to represent different terrain conditions, ecosystem types (land cover types, ranging from desert, alpine steppe to cropland), and climate zones on the Tibetan Plateau (Table 1). Each station provides unique insights into dif-

ferent atmospheric and environmental aspects, enhancing the overall representativeness of the study. MAWORS is located in the westerly climate zone and has a dry and cold climate. This site provides essential data on the impact of westerly driven weather [43]. The QOMS is located in a semi-arid plateau monsoon climate [44] at 4298 m.a.s.l. and 30 km from the northern boundary of Mt. Everest. It is dominated by alpine Gobi desert, relatively flat and open terrain characterized mainly by bare ground and sparse and short vegetation. MAWORS is located close to Muztagh Mountain and Karakuli Lake and lies at 3668 m.a.s.l. The NAMORS is situated on the southeast bank of Namco Lake, surrounded by the Nyenchen Tanglha Mountains and has an elevation of 4730 m.a.s.l. It is classified as an alpine meadow and belongs to the semi-arid plateau monsoon climate zone. The Dali Station, situated at 1999 m.a.s.l., nestles between the Cangshan Mountains to the west and Erhai Lake to the east. This location allows sampling a crucial water vapor transport channel in Hengduan Moutains on the southeastern edge of the Tibetan Plateau. Dali station is located in the windward zone of the Southwest Monsoon of the Bay of Bengal, belonging to the subtropical highland monsoon climate type. Detailed information about the locations and the instruments for Dali NAMORS, MWWORS, and QOMS stations can be found in [45,46].

Table 1. Geographic characteristics of the four stations with radiation measurements over Tibetan Plateau (30 m resolution slope and aspect derived from 30 m resolution ASTER-GDEM2; 1 km slope and aspect resampled from 30 m resolution slope and aspect).

Station Name	Latitude	Longitude	Elevation (m.a.s.l.)	Slope (30 m/1 km)	Aspect (30 m/1 km)	Land Cover	Soil Type
MAWORS	38.42°N	75.03°E	3668	5°/19°	119°/106°	Alpine desert	Sand and gravel
NAMORS	30.77°N	90.96°E	4730	3°/5°	256°/155°	Alpine steppe	Sandy and loam
QOMS	28.36°N	86.95°E	4298	7°/8°	45°/172°	Alpine desert	Sand and gravel
Dali	25.72°N	100.19°E	1990	3°/3°	309°/109°	Farmland	Paddy soil

We used time-averaged observations with a temporal resolution of 30 min at QOMS, MAWORS and NAMORS station and or 1 h at Dali station. Every station provides distinct observations on various atmospheric and land surface processes. The surface radiation components include the incoming and outgoing shortwave and longwave radiations. The ground measurements of surface shortwave albedo were obtained as the ratio of shortwave upwelling radiation to shortwave downwelling radiation.

Although the four stations are sparsely distributed, their strategic locations in diverse ecological and climatic settings across the Tibetan Plateau, coupled with the comprehensive analysis of daily atmospheric conditions over a year at the MODIS Aqua and Terra overpass time, provide a robust and representative dataset for our study. We believe that our evaluation covered the solar irradiance variability across this unique and complex region.

2.2. Satellite Data

The Terra and Aqua satellites utilize MODIS sensors to capture images in 36 spectral bands ranging from 0.62 µm to 14.385 µm. These images have a broad ground swath of approximately 2330 km and different spatial resolutions of 250 m, 500 m, and 1 km depending on the spectral band. The MODIS level 1B data undergo radiometric calibration, while the level 2 data are atmospherically corrected and formatted in an ungridded orbital swath, resulting in a product that spans five minutes. The Terra and Aqua products will be referred to collectively with the identifiers "MOD" and "MYD", respectively. For this study, MODIS Aqua and Terra data were employed, and the atmospheric products (e.g., MOD04/MYD04 L2, MOD05/MYD05 L2, MOD06/MYD06 L2, and MOD07/MYD07 L2) and the calibrated radiance product (MOD021KM/MYD021KM) from Table 2 were used as input data. The first seven spectral bands of MOD021KM/MYD021KM are used to estimate shortwave TOA radiance in this study. The instantaneous MODIS TOA spectral radiance was converted to TOA total shortwave radiance according to narrowband-to-

broadband conversion method [47]. The study utilized eight variables—namely, aerosol optical depth (AOD), precipitable water content, ozone optical depth, surface pressure, cloud top pressure, cloud fraction, and cloud optical depth, all obtained from MODIS atmospheric data products—to estimate atmospheric transmittance. The MOD03/MYD03 provided the geolocation of the observations. The MODIS BRDF/Albedo MCD43A3 C6.1 dataset, available from the NASA Land Processes Distributed Active Archive Center (LP DAAC), produces albedo quantities at a resolution of 500 m in a sinusoidal projection. The MODIS MCD43A2 C6.1dataset is BRDF/Albedo) quality dataset is produced daily using 16 days of Terra and Aqua MODIS data at 500 m resolution for the corresponding 16-day MCD43A3 BRDF/Albedo dataset. The MCD43A2 contains individual band quality and observation information for the MODIS land bands 1–7, along with the overall BRDF/Albedo quality information. These quantities have been produced daily since 2000 with a synthesis period of 16 days, using data from both the Terra and Aqua satellites.

Table 2. MODIS level 2 data products and DEM data used in this study.

Product Short Name	Product Name	Spatial Resolution	Temporal Resolution	Data Type
MOD021km/MYD021km	Calibrated Radiance	1 km	5 min	EV_250_Aggr1km_RefSB EV_500_Aggr1km_RefSB
MOD03/MYD03 L2	Geolocation dataset	1 km	5 min	Longitude/latitude
MOD04/MYD04 L2	Aerosol optical thickness	10 km	5 min	Corrected optical depth land
MOD05/MYD05 L2	Total precipitable water vapor	5 km	5 min	Water vapor NIR retrieval
MOD06/MYD06 L2	Cloud	1 km or 5 km	5 min	Surface pressure Cloud top pressure Cloud fraction Cloud optical thickness
MOD07/MYD07 L2	Atmosphere profile	5 km	5 min	Total ozone
ASTER-GDEM2	DEM	30 m	-	DEM

The ASTER-GDEM2 dataset was used for calculating topographic parameters, i.e., slope, aspect, SVF (sky-view factor) and TVF (terrain-view factor) [48,49], which is one of the most widely used high-resolution digital topographic datasets to date. The 30 m resolution ASTER-GDEM2 data were averaged to estimate the mean elevation of each 1 km $\times$ 1 km grid, i.e., the same spatial resolution as the MODIS surface reflectance data. The slope, aspect, SVF and TVF of the terrain were retrieved at a 30 m resolution from the DEM generated using the data acquired by ASTER-GDEM2 data and then averaged to 1 km resolution.

3. Method

In this study, we retrieved surface albedo by calculating first all the relevant radiative fluxes under all sky conditions, taking into account the terrain effects on both the incoming and the reflected radiant energy. The procedure includes four steps: (1) estimating instantaneous surface solar irradiance (SSI) and its four components under all sky conditions over rugged terrain using a physically-based model [42,50] (see Section 3.1); (2) estimating the instantaneous at-surface upwelling directional radiance under all sky conditions in rugged terrain [24,51] (see Section 3.2); (3) estimating land surface reflectance under clear and cloudy sky on a rugged surface (see Section 3.3); and (4) estimating the surface albedo of rugged terrain [52] (see Section 3.4). The workflow used to retrieve the surface albedo is illustrated schematically in Figure 2. The detailed methods are described in the following sections.

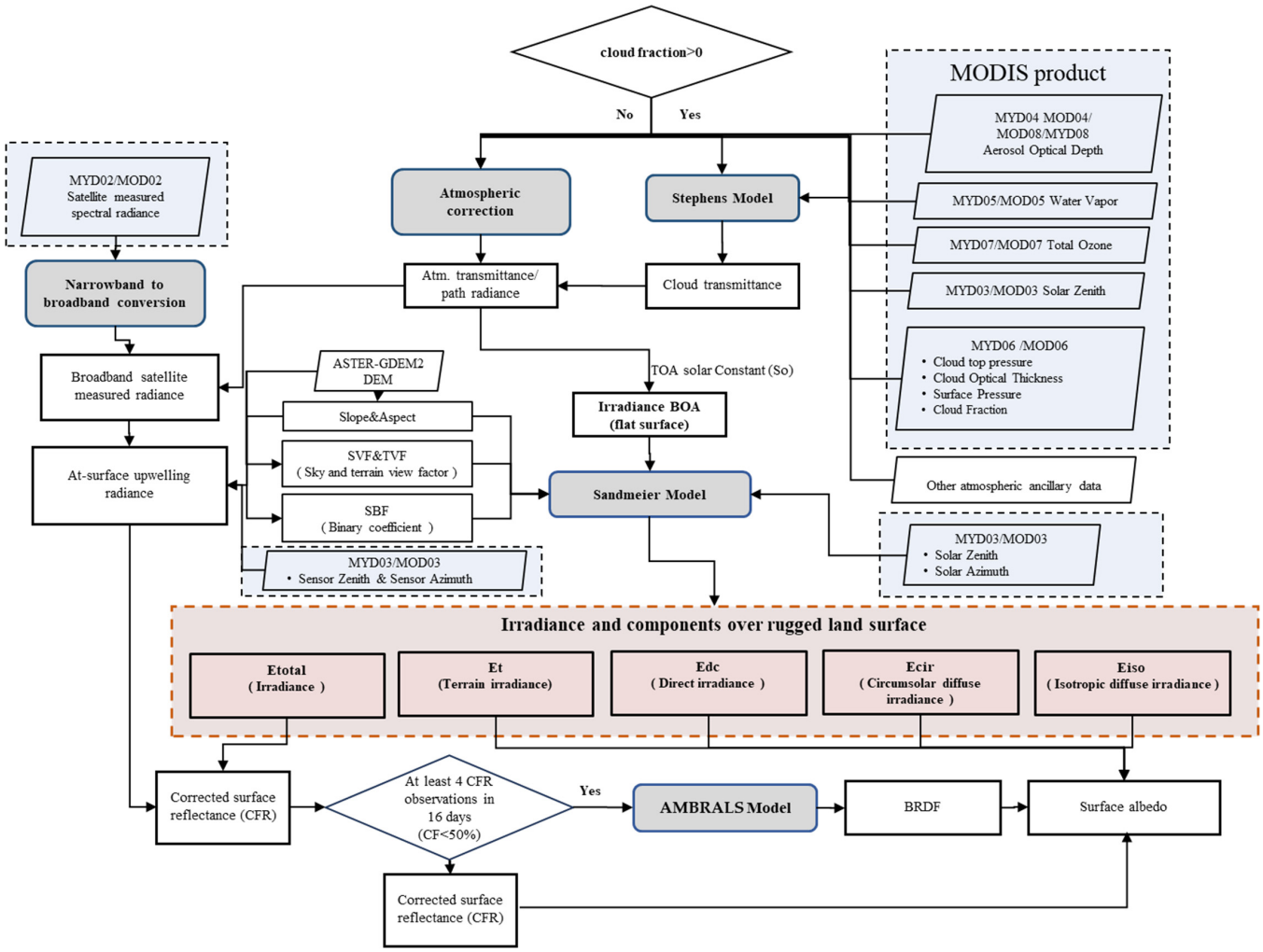

Figure 2. Schematic diagram of the workflow for the retrieval of the surface albedo in rugged terrain.

3.1. Estimation of Surface Solar Irradiance under Full Sky Conditions over Rugged Terrain

Over rugged terrain, the temporal and spatial distribution of surface solar irradiance (SSI) is the result of complex interactions among the incoming solar beam, the atmosphere, and the surface. At the bottom of the atmosphere (BOA), the SSI on a rugged terrain element includes four components, i.e., direct irradiance (E_{dc}, W/m^2), isotropic diffuse irradiance (E_{iso}, W/m^2), circumsolar diffuse irradiance (E_{cir}, W/m^2) and terrain irradiance (E_t, W/m^2) [42,50] and can be described as:

$$E_{total} = E_{dc} + E_{cir} + E_{iso} + E_t \quad (1)$$

where E_{total} (W/m^2) is the at-surface solar irradiance (SSI); E_{dc} (W/m^2) is the solar radiation directly reaching the surface through the atmosphere in rugged terrain; E_{cir} (W/m^2) is the scattering of direct sunlight in the atmosphere, and the effect of topography can be modeled using the same method used for direct irradiance; E_{iso} (W/m^2) is a function of the proportion of the sky hemisphere not obstructed by the topography; E_t (W/m^2) is the irradiance reflected by the terrain surrounding the observed facet. We have proposed a method of estimating the four components in Equation (1) under full sky conditions over rugged terrain [51]; a brief description is given below.

3.1.1. SSI under Clear Sky Conditions over Rugged Terrain

Under clear sky conditions, the direct solar irradiance is influenced by the slope and azimuth of the observed terrain facet and of the surrounding terrain. Solar radiation is

absorbed by water vapor, ozone and other uniformly mixed gases, while aerosols either scatter or absorb radiation [53]. In mountainous regions, two primary factors influence the irradiance onto the observed facet: the orientation of the observed facet relative to the Sun beam and the impact of the facet orientation combined with the surrounding terrain. Part of the radiation scattered in the atmosphere can reach the rugged surface as diffuse irradiance. The direct irradiance (E_{dc}, W/m^2), anisotropic circumsolar diffuse irradiance (E_{cir}, W/m^2), isotropic diffuse irradiance (E_{iso}, W/m^2), a function of the proportion of the sky hemisphere not obstructed by the topography) and terrain irradiance for a tilted facet under clear sky conditions (E_t, W/m^2), a complex term, as it consists of both the direct and diffuse irradiance reflected from surrounding terrain [54,55]) can be described by the following equations:

$$E_{dc} = \Theta E_d \frac{cos\theta_i}{cos\theta_s} \tag{2}$$

$$E_{cir} = E_f k \frac{cos\theta_i}{cos\theta_s} \tag{3}$$

$$E_{iso} = E_f (1 - k) V_d \tag{4}$$

$$E_t = \left(E_d + E_f\right) V_t \rho_{adj} \tag{5}$$

where Θ is a binary coefficient introduced by [45] that controls the cast shadows and is set to zero for a facet in the shadow and to one for a sunlit facet. θ_i is the solar incident angle between the normal to the facet and the Sun line of illumination (LoI). Both θ_i and Θ are derived from ASTER-GDEM2. θ_s is the solar zenith from MOD03/MYD03 products. k is the ratio of direct irradiance on a flat surface (E_d, W/m^2) to the irradiance at the top of the atmosphere, which is also called Hay's anisotropy index [56]; ρ_{adj} is the surface reflectance of the adjacent objects. V_d is the sky view factor (SVF), which is defined as the ratio of the sky portion seen from a specific facet to that on an unobstructed horizontal facet. V_t is the terrain view factor (TVF), defined as the portion of hemisphere overlying the observed facet and obstructed by the surrounding terrain. The sky view and terrain view factors are calculated using the analytical algorithm developed by [48]. The sky view and terrain view factors are also derived from the ASTER-GDEM2.

In Equations (2)–(5), E_d (W/m^2) is the direct irradiance on flat surface and E_f (W/m^2) is the diffuse irradiance on flat surface, and they are calculated as:

$$E_d = E_0 \cdot cos\ (\theta_s) \cdot T_B \tag{6}$$

$$E_f = E_0 \cdot cos\theta_s \cdot T_D \tag{7}$$

where E_0 (W/m^2) is the extraterrestrial solar irradiance, T_B is the direct beam transmittance, and T_D is the diffuse transmittance under clear sky introduced by [57]. They are calculated as:

$$E_0 = S_0 \cdot SE_d \tag{8}$$

$$T_B = \tau_o \cdot \tau_w \cdot \tau_g \cdot \tau_r \cdot \tau_a \tag{9}$$

$$T_D = 0.5\tau_o \cdot \tau_w \cdot \tau_g \cdot (1 - \tau_a \cdot \tau_r) \tag{10}$$

where S_0 (W/m^2) is the solar constant (1367 W/m^2). SE_d is Sun–Earth distance. Transmittance factors ($\tau_r, \tau_a, \tau_o, \tau_w, \tau_g$) introduced by [57] are influenced by five radiation-damping processes under clear sky conditions: (1) Rayleigh scattering, (2) aerosol extinction, (3) ozone absorption, (4) water vapor absorption, and (5) permanent gas absorption.

The input variables for calculation of transmittance factor ($\tau_r, \tau_a, \tau_o, \tau_w, \tau_g$) are the surface pressure, precipitable water, optical thickness of the ozone layer, ozone thickness, and AOD, which can be obtained from MODIS data products (Table 2).

3.1.2. SSI under Cloudy Sky Conditions over Rugged Terrain

Under cloudy conditions, cloud tops reflect a fraction of the solar radiation back into space while allowing the rest to pass through. In this study, the influence of clouds on radiation is modeled using a parameterization method described in detail in [30,58]. This method categorizes the solar shortwave range into two broad bands: 0.30–0.75 μm and 0.75–4 μm, and is designed to estimate the reflection, transmission, and absorption of radiation by clouds within these bands. The direct irradiance ($E_{dc}{}'$, W/m^2) is direct irradiance in the cloud-free fraction of a pixel. The isotropic diffuse irradiance ($E_{iso}{}'$, W/m^2) in a pixel is composed of three components: the isotropic diffuse irradiance in the cloudless fraction, the isotropic diffuse irradiance transmitted by the clouds, and the isotropic diffuse irradiance scattered by the clouds. The circumsolar diffuse irradiance ($E_{cir}{}'$, W/m^2) in a pixel is composed of the circumsolar diffuse irradiance in the cloudless part and the circumsolar diffuse irradiance scattered by the clouds.

Under cloudy conditions, the direct irradiance ($E_{dc}{}'$, W/m^2), anisotropic circumsolar diffuse irradiance ($E_{cir}{}'$, W/m^2), isotropic diffuse irradiance ($E_{iso}{}'$, W/m^2), and terrain irradiance for a tilted facet under cloudy sky conditions can be described by the following equations [43]:

$$E_{dc}{}' = (1 - cf) \times E_{dc} \tag{11}$$

$$E_{iso}{}' = E_f(1 - cf)(1 - k)V_d + T_B{}'E_0 cf cos\theta_s V_d + (1 - T_B)E_{iso}cf \tag{12}$$

$$E_{cir}{}' = E_f(1 - cf)k\frac{cos\theta_i}{cos\theta_s} + \left(1 - T_B{}'\right) E_{cir}cf \tag{13}$$

$$E_t{}' = \left(E_{dc}{}' + E_f{}'\right)V_t\rho_{adj} \tag{14}$$

$$E_f{}' = T_B{}'E_0\, cos\theta_i cf + (1 - cf)E_f \tag{15}$$

$$T_B{}' = \tau_o{\cdot}\tau_w{}'{\cdot}\tau_g{}'{\cdot}\tau_r{}'{\cdot}\tau_a{\cdot}\tau_c \tag{16}$$

where τ_c is the cloud transmittance according to [30]. τ_c is estimated from cloud optical thickness from MOD06/MYD06; cf is the cloud fraction from MOD06/MYD06, defined as the fraction of each pixel covered by clouds and determines the impact of the clouds on the solar radiation. $E_{dc}{}'$ is estimated as a proportion of clear-sky direct irradiance under cloudy sky conditions. $E_{iso}{}'$ is the isotropic diffuse irradiance under cloudy sky conditions. $E_{cir}{}'$ is circumsolar diffuse irradiance under cloudy sky. $E_t{}'$ is the terrain irradiance under cloudy sky conditions. $E_f{}'$ is the diffuse component of irradiance on a horizontal surface under cloudy sky conditions. $T_B{}'$ is the total transmittance under cloudy conditions. Transmittance factors ($\tau_w{}'$, $\tau_g{}'$, $\tau_r{}'$) under cloudy conditions were introduced by [42].The input variables for estimation of transmittance factors ($\tau_w{}'$, $\tau_g{}'$, $\tau_r{}'$) under cloudy conditions include not only the surface pressure, precipitable water, optical thickness of the ozone layer, ozone thickness, and AOD from the MODIS data product but also cloud top pressure provided by MOD06/MYD06 product (Table 2).

3.2. At-Surface Upwelling Radiance under Clear and Cloudy Sky in Rugged Terrain

In this study, at-surface upwelling radiance was estimated and then used to obtain the bidirectional surface reflectance, which is the key radiative variable in the estimation of at-surface reflectance as Ross–Li model input data for retrieving surface albedo. The surface reflected radiant exitance was divided by the SSI to derive surface reflectance in a specific direction towards the sensor (see Section 3.1). The at-surface upwelling radiance L_{BOA} ($W/m^2/sr$) was estimated from the at-satellite TOA radiance ($W/m^2/sr$) by taking into account the effects of the atmosphere described above.

3.2.1. At-Surface Upwelling Radiance under Clear Sky in Rugged Terrain

Terrain characteristics not only affect SSI but also radiance reflected by the surface under different atmospheric conditions. We used a simple model to remove the reflected radiance of the surrounding terrain irradiance by surface following previous study [21]. This

model estimates the at-surface upwelling radiance in rugged terrain, taking into account topographic influence. Under clear sky conditions, the at-sensor TOA radiance from a target pixel observed by MODIS (provided by the MYD02/MOD02 products) is composed of (1) the at-surface upwelling radiance of the pixel (L_{BOA}) attenuated by the atmosphere, (2) the irradiance from the surrounding terrain that is reflected by the observed facet and attenuated by the atmosphere (surrounding terrain contribution ($L_{TOA,\ topo\_neighbor}$), and (3) the atmospheric contribution (L_P) and is expressed as:

$$L_{TOA} = (T_B + T_D)\ cos\theta_v\ L_{BOA} + L_{TOA,\ topo\_neighbor} + L_P \tag{17}$$

where L_{TOA} (W/m^2/sr) is the observed at-sensor TOA radiance made available in the MYD02/MOD02 product, $L_{TOA,topo\_neighbor}$ (W/m^2/sr) is the TOA value of the irradiance from the surrounding topography that is reflected by the observed pixel surface, and L_p (W/m^2/sr) is the path radiance along the satellite observation direction under clear sky conditions as estimated using MODTRAN. The spectral TOA radiance (W/m^2/sr) in MOD02/MYD02 is converted into shortwave TOA radiance according to [47]. θ_v is the satellite observation zenith angle from the MOD03/MYD03 product. Assuming that at TOA, the proportion of the terrain irradiance to the total surface solar irradiance is the same as the proportion of terrain radiance to observed radiance at BOA, $L_{TOA,\ topo\_neighbor}$ can be estimated as:

$$L_{TOA,\ topo\_neighbor} = \frac{E_t}{E_{total}} \cdot (L_{TOA} - L_p) \tag{18}$$

Therefore, under clear sky conditions, the at-surface upwelling radiance of the pixel, L_{BOA}, is calculated by deducting the contributions from surrounding terrain and the atmosphere (combining Equations (17) and (18)) and expressed as:

$$L_{BOA} = \frac{(L_{TOA} - L_p)}{(T_B + T_D)cos\theta_v} - \frac{E_t}{E_{total}} \left[\frac{(L_{TOA} - L_p)}{(T_B + T_D)cos\theta_v} \right] \tag{19}$$

The first term of Equation (19) is the surface reflected radiance at observation angles at the bottom of atmosphere after atmospheric correction. The second term of Equation (19) is the irradiance from surrounding topography reflected by the observed surface facet.

3.2.2. At-Surface Upwelling Radiance under Cloudy Sky in Rugged Terrain

Under cloudy sky conditions, the at-sensor TOA radiance includes the radiation reflected by the land surface and transmitted by clouds, path radiance, the radiation scattered by the surroundings of the observed target and the radiation reflected by clouds. In order to increase the number of valid retrievals of surface reflectance, we estimated the at-surface shortwave upwelling radiance under cloudy sky conditions ($L_{BOA}{}'$, W/m^2/str) as:

$$L_{BOA}{}' = \frac{(L_{TOA} - L_p)}{T_{all}{}'} - \frac{E_t}{E_{total}} \left[\frac{\left(L_{TOA} - L_p - \frac{E_{cf}}{\pi}\right)}{T_{all}{}'} \right] \tag{20}$$

$$T_{all}{}' = \left[(T_B + T_D)(1 - cf) + T_B{}' cf\right] cos\theta_v \tag{21}$$

$$E_{cf} = E_0 \rho_{cld} \times cf(\tau_{oz}\overline{\tau_r})^2 \tau_c cos_{\theta_v} cos\theta_s \tag{22}$$

where $T_{all}{}'$ is atmospheric transmittance under cloudy sky at observation angle θ_v. E_{cf} (W/m^2) is the cloud reflected radiative flux observed by a satellite at TOA. ρ_{cld} is the cloud reflectance from [30].

3.3. Estimating Land Surface Reflectance under Clear and Cloudy Sky Conditions on a Rugged Surface

At-surface reflectance is the ratio of at-surface upwelling radiant exitance at given incident and observation angles to SSI. The at-surface reflectances under clear and cloudy sky conditions are:

$$\rho_{BOA} = \frac{L_{BOA}\,\pi}{E_{dc} + E_{cir} + E_{iso} + E_t} \tag{23}$$

$$\rho_{BOA}{}' = \frac{L_{BOA}{}'\,\pi}{E_{dc}{}' + E_{cir}{}' + E_{iso}{}' + E_t{}'} \tag{24}$$

where ρ_{BOA} is the shortwave surface reflectance under clear sky and $\rho_{BOA}{}'$ is the shortwave surface reflectance under cloudy sky.

3.4. Retrieval of Surface Albedo over Rugged Terrain

Rugged terrain alters the ratio of direct, diffuse, and terrain-reflected radiations [59]. The actual surface albedo quantifies the fraction of the sunlight energy reflected by the surface of the Earth.

We used two complementary methods to retrieve the surface albedo: (1) if there are at least three observations with cf $\leq$ 50% within a 16-day window, we construct the BRDF using the same method as in the MODIS MCD43 BRDF/albedo algorithm; (2) if there are fewer than three observations with cf $\leq$ 50% within a 16-day window (cloudy conditions), we estimate the surface albedo as the ratio of the at-surface upwelling radiant exitance to the SSI.

In the first method, the surface albedo (α) of rugged terrain can be written as:

$$\alpha = \frac{E_{dc}\rho_{dh}(\theta_i, \varphi_i; \theta_v, \theta\varphi_v,\ 2\pi) + (E_{cir} + E_{iso})\rho_{hh}(\theta_i, \varphi_i, 2\pi; 2\pi) + E_t\rho_{hh} + (E_{cir} + E_{iso})\rho_{hd}(\theta_i, \varphi_i, 2\pi; \theta_v, \varphi_v)}{E_{total}} \tag{25}$$

where $\rho_{dh}(\theta_i, \varphi_i; \theta_v, \varphi_v, 2\pi)$, also called the black-sky albedo (BSA), is the directional-hemispheric reflectance, which is the hemispheric integral of the radiance reflected by a surface into the view hemisphere when illuminated by a point-like direct illumination source. $\rho_{hd}(\theta_i, \varphi_i, 2\pi; \theta_v, \varphi_v)$ is the reflectance for the hemispheric irradiance in a specific direction of observation (line of sight, LoS) and is an integral of the bidirectional reflectance over all incidence angles and is equal to the hemispherical directional reflectance factor (HDRF). $\rho_{hh}(\theta_i, \varphi_i, 2\pi; 2\pi)$ is the bi-hemispheric reflectance, also called the white-sky albedo (WSA). Although $\rho_{dh}(\theta_i, \varphi_i; \theta_v, \varphi_v, 2\pi)$ and $\rho_{hd}(\theta_i, \varphi_i, 2\pi; \theta_v, \varphi_v)$ are defined from different perspectives of reflectance measurement, their values can be considered approximately equivalent under many practical circumstances due to their similar roles in characterizing the reflective properties of the surface [60].

The $\rho_{dh}(\theta_i, \varphi_i; \theta_v, \varphi_v, 2\pi)$ and $\rho_{hh}(\theta_i, \varphi_i, 2\pi; 2\pi)$ are as follows:

$$\begin{aligned}\rho_{dh}(\theta_i, \varphi_i; \theta_v, \varphi_v, 2\pi) = f_{iso}\left(g_{0iso} + g_{1iso}\theta^2 + g_{2iso}\theta^3\right)\\ + f_{vol}\left(g_{0vol} + g_{1vol}\theta^2 + g_{2vol}\theta^3\right)\\ + f_{geo}\left(g_{0geo} + g_{1geo}\theta^2 + g_{2geo}\theta^3\right)\end{aligned} \tag{26}$$

$$\rho_{hh}(\theta_i, \varphi_i, 2\pi; 2\pi) = f_{iso}g_{iso} + f_{vol}g_{vol} + f_{geo}g_{geo} \tag{27}$$

where f_k (k = iso, vol, geo) is BRDF model kernel weights in kernel-driven BRDF model. g_{jk} (j = 0, 1, 2; k = iso, vol, geo) and g_k coefficients are taken from [10].

The BRDF quantifies the angular distribution of radiance reflected by an illuminated surface [61]. We used an RTLSR-kernel-driven BRDF model that linearly combines three kernels: isotropic scattering, volume scattering, and geometric optics scattering according to the algorithm of the MCD43 BRDF/albedo product [62]. The Ross–Li kernel-driven BRDF model equation is:

$$R(\theta_i, \theta_v, \varphi_i, \varphi_v) = f_{iso} + f_{vol}k_{vol}(\theta_i, \theta_v, \varphi_i, \varphi_v) + f_{geo}k_{geo}(\theta_i, \theta_v, \varphi_i, \varphi_v) \tag{28}$$

where $R(\theta_i, \theta_v, \varphi_i, \varphi_v)$ is the at-surface bidirectional reflectance, f_{iso} is the coefficient of the isotropic term, k_{vol} is the volume scattering term from the Ross–Thick kernel, k_{geo} is the geometrical optical scattering term of the Li–Ross kernel, f_{vol} is the coefficient of k_{vol}, and f_{geo} is the coefficient of k_{geo}.

Given the at-surface reflectance ρ_{BOA} at specific incident and view angles obtained from Equations (23) and (24) under clear and cloudy sky conditions, we can derive analytical solutions for the model parameters f_k in Equation (28) by minimizing a least squares error function as applied in the MCD43 BRDF/albedo algorithm (when applying $\frac{\partial e^2}{\partial f_k} = 0$):

$$e^2 = \frac{1}{d} \sum_{i=1}^{n} \frac{[\rho_{BOA,i}(\theta_{in}, \theta_{vn}, \varphi_{in}, \varphi_{vn}) - R_i(\theta_{in}, \theta_{vn}, \varphi_{in}, \varphi_{vn})]^2}{\omega_i} \quad (29)$$

where n is the number of observations (the minimum number of observations is taken as 3 in our method), d is degree of freedom (number of observations minus number of unknown parameters), and ω_i is a weight given to each respective observation. ρ_{BOA} is estimated by Equations (23) and (24).

If the number of observations with cf $\leq$ 50% within a 16-day window is insufficient to determine the parameters of the BRDF model, we apply the second method to estimate the surface albedo as the ratio of the at-surface upwelling radiance to the SSI from Equations (23) and (24).

Once all the components in Equation (25) are estimated through the above procedures, land surface albedo over rugged terrain under clear and cloudy sky conditions is obtained.

3.5. Validation Approach

We used four error metrics for the evaluation of our retrievals by comparison with in situ observations: the bias (Bias), root mean square error (RMSE), mean absolute percentage error (MAPE), and correlation coefficient (R), which are calculated as follows:

$$\text{Bias} = \sum_{i=1}^{n} (x_i - y_i) \quad (30)$$

$$\text{RMSE} = \sqrt{\frac{1}{n} \sum_{i=1}^{n} (x_i - y_i)^2} \quad (31)$$

$$\text{MAPE} = \frac{1}{n} \sum_{i=1}^{n} \left| \frac{x_i - y_i}{x_i} \right| \quad (32)$$

$$R = \frac{\sum_{i=1}^{n} (x_i - \overline{x}) \times (y_i - \overline{y})}{\sum_{i=1}^{n} (x_i - \overline{x})^2 \times (y_i - \overline{y})^2} \quad (33)$$

where x_i is the in situ observation value, y_i is the value estimated using the method developed in this study, $\overline{x}$ is the average observation value, $\overline{y}$ is the average estimated value, and n is the number of estimates and measurements.

4. Results

The method proposed in Section 3 and the data introduced in Section 2 were applied to estimate both instantaneous at-surface upwelling shortwave radiance and surface albedo taking into account the coupled effects of the topography and atmosphere at 1 km spatial resolution on the Tibetan Plateau. The method was evaluated against in situ daily measurements recorded daily at the Dali, NAMORS, MAWORS, and QOMS stations on the Tibetan Plateau in 2018. This validation revealed that at-surface upwelling estimates and the surface albedo retrieval are in satisfactory agreement with the ground observations (Sections 4.2 and 4.3) and our approach clearly improved the spatial and temporal coverage of the albedo retrievals (Section 4.4).

4.1. Number of Valid Observations in the Improved Method versus MODIS Product

Both our surface albedo retrieval method and the MODIS albedo algorithm (MCD43A3) require at least 4 valid surface reflectance observations every 16 days to construct the BRDF for surface albedo inversion. The MODIS MCD43A2 product provides the BRDF/Albedo band quality and information on the days of valid observation of surface reflectance within each 16-day period for MODIS bands 1 to 7. The advantage of our method over the MODIS surface albedo algorithm can then be best documented by comparing the number of valid surface reflectance observations. This comparison was made for the Dali, MAWORS, NAMORS, and QOMS stations (Figure 3). For the MODIS MCD43A2 product, the number of valid observations is the sum of the number of valid daily surface reflectance (clear sky) observations that can be used to successfully retrieve daily surface albedo within each 16-day moving window in each month. For our method, we calculated the number of valid observations in each month in the same way but used the conditions of the cloud fraction less than 50% (other than totally clear sky as required by the MODIS algorithm), taking into account the accuracy in the estimating cloud reflectance and transmittance (see Section 4.2). The number of valid observations with our method was, as expected, much higher than with the MODIS algorithm, i.e., 200% higher at Dali, 66% higher at QOMS, 100% higher at MAWORS, and 40% higher at NAMORS station. This difference is that this lacks the advantage of estimating the at-surface upwelling radiance under cloudy conditions as our method does. The performance of this advantage of our method is evaluated in the next Section 4.2. At Dali Station, the absence of days, with zero cloudy days in July and the presence of clear sky conditions only on certain days in August, highlighted the limitations of the MODIS algorithm in providing more effective albedo retrievals. The situation at QOMS Station mirrors that at Dali Station.

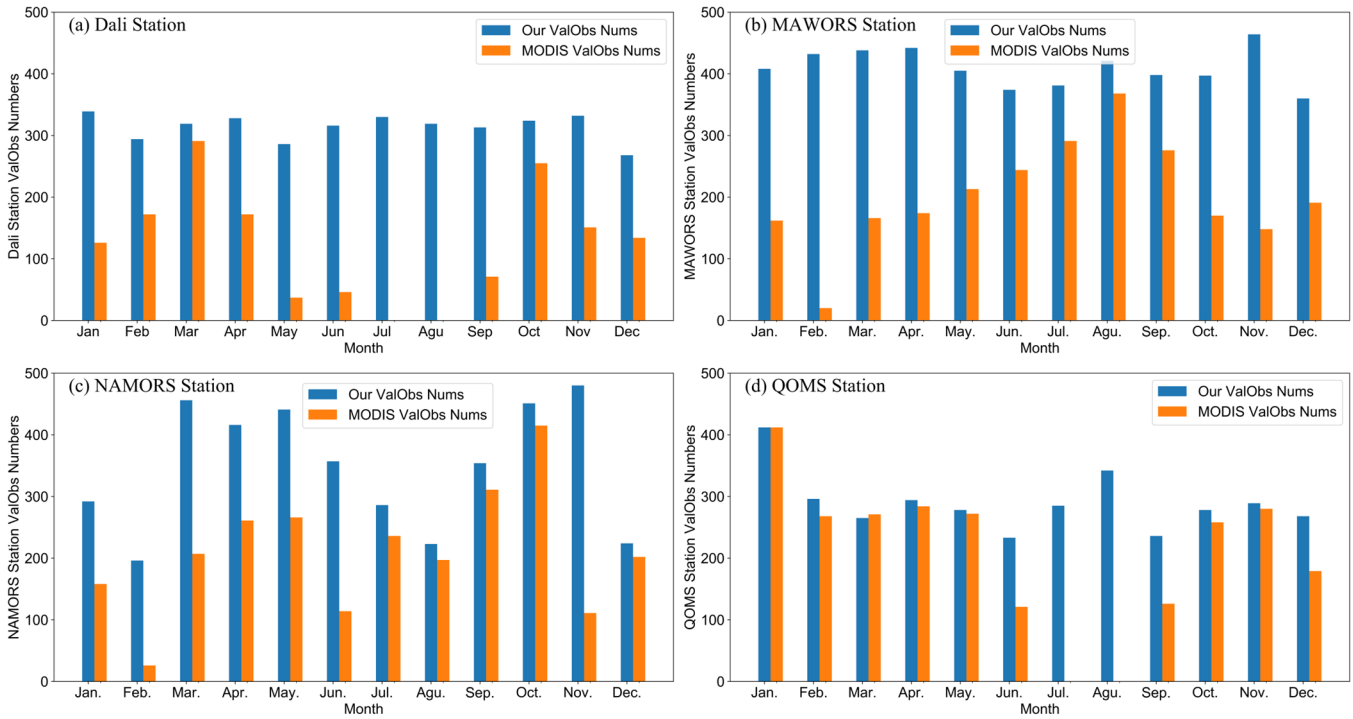

Figure 3. Comparison of the monthly distribution of the sum of the number of valid daily surface reflectance observations (ValObs) between our method and MODIS MCD43A2 that can be used for successful retrieval of daily surface albedo within each 16-day moving window at the four stations on the Tibetan Plateau in 2018: (**a**) Dali Station, (**b**) MAWORS Station, (**c**) NAMORS Station, and (**d**) QOMS Station.

4.2. Evaluation of Retrieved At-Surface Upwelling Radiance

Our method relies on the estimation of the at-surface upwelling radiance under all sky conditions, which requires the estimation of cloud reflectance and transmittance, in addition to atmospheric absorption and scattering and to terrain irradiance (see Section 3.2). We compared our estimation of at-surface upwelling radiance with a set of ground observations at the four stations on the Tibetan Plateau in 2018. We used time averaged observations of a temporal interval of 30 min (QOMS, MAWORS, and NAMORS) or 1 h (Dali). We applied four error metrics—BIAS, MAPE, RMSE, and R—calculated using Equations (30)–(33). Better estimates of the at-surface upwelling radiance were obtained for MAWORS, NAMORS, and QOMS than for Dali when the cloud fraction (CF) of the pixel at the ground site measured by MOD06/MYD06 was less than 50% (Figure 4).

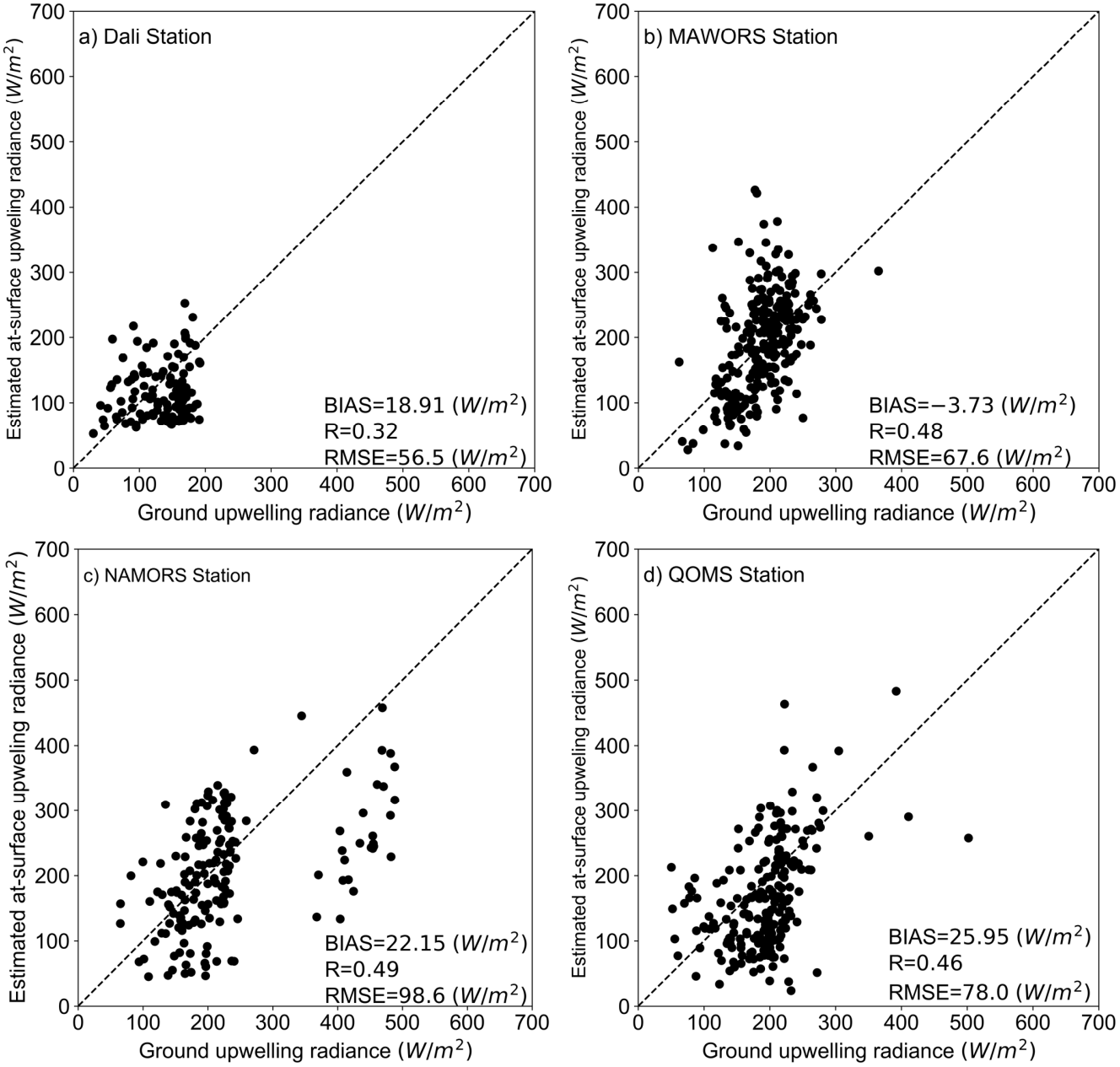

Figure 4. Validation of the instantaneous at-surface upwelling estimated using the method developed in this study when CF < 50% by comparison with the ground observations at Dali, NAMORS, MAWORS, and QOMS stations on the Tibetan Plateau in 2018 during the MODIS Terra and Aqua overpass time.

The estimates of at-surface upwelling radiance at MAWORS, NAMORS, QOMS, and Dali stations were also evaluated at different cloud fractions (Figure 5). Five cloud fraction bins were considered: CF = 0%, 0% < CF ≤ 20%, 20 < CF ≤ 50%, 50% < CF ≤ 75%, and 75% < CF ≤ 100%. Under clear sky conditions (CF = 0%) and low cloud fraction (0% < CF ≤ 20%), all stations have relatively low MAPE values, indicating the higher accuracy of the estimates. As the cloud fraction increases (20% < CF ≤ 50% and 50% < CF ≤ 75%), all stations show varying increases in MAPE, indicating that the presence of clouds makes the estimates of at-surface upwelling radiance more challenging. At the highest cloud fraction level (75% < CF ≤ 100%), there is a significant increase in MAPE for all stations, particularly for QOMS and NAMORS. This indicates that estimation errors increase significantly with high cloud coverage, suggesting that the current parameterization of cloud reflectance and transmittance should be improved to better deal with nearly complete cloud cover conditions.

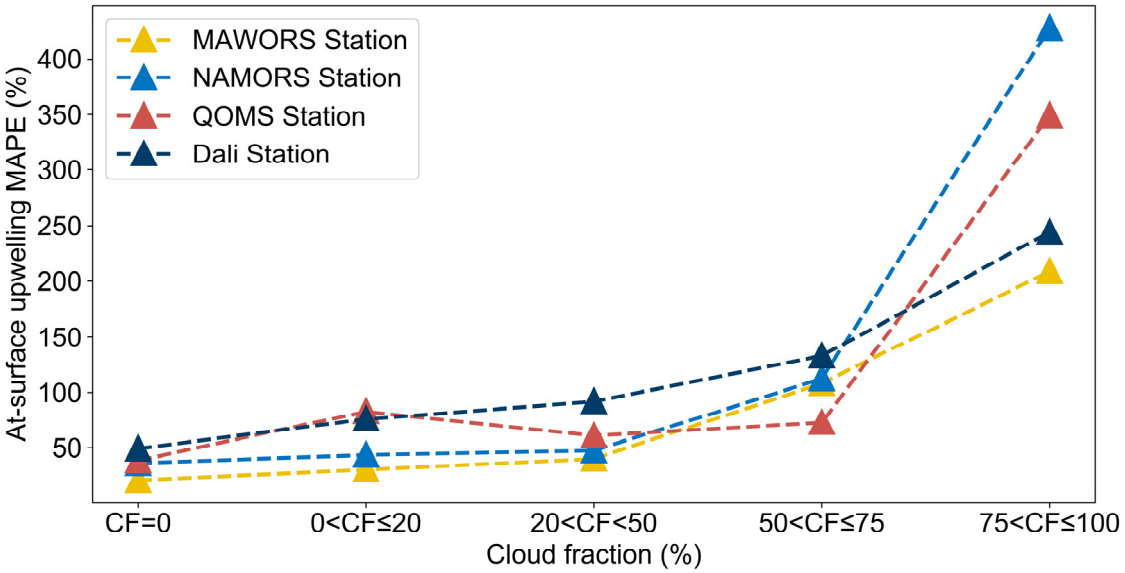

Figure 5. The MAPE for at-surface upwelling radiance estimates at different cloud fractions at Dali, MAWORS, NAMORS, and QOMS stations on the Tibetan Plateau in 2018.

Using the method described here, we estimated instantaneous at-surface upwelling radiance corresponding to the overpass time applied to the MODIS orbital products, i.e., a spatial map was produced every 5 min with a spatial resolution of 1 km. Figure 6 shows an example on 2 January 2018, with large cloud cover over the Tibetan Plateau, to demonstrate the ability of our method to provide more valid estimates of at-surface upwelling radiance.

4.3. Evaluation of Retrieved Surface Albedo

We compared our shortwave surface albedo with the shortwave WSA and BSA of MODIS (MCD43A3) and with ground measurements of surface albedo at four stations on the Tibetan Plateau: Dali, MAWORS, NAMORS, and QOMS (Figure 7). The MODIS retrievals apply to clear sky only, and the MODIS albedo products do not include blue-sky albedo retrievals. In general, the blue-sky albedo is computed by linear interpolation of WSA and BSA on the basis of the fraction of diffuse skylight [63], but as shown in Section 3.4, the blue-sky albedo depends nonlinearly on BSA and WSA in a rugged terrain. We compared our broadband albedo retrievals with both MODIS WSA and BSA (Figure 7) with the ground measurements. Our method led to a significant reduction in RMSE at the four observation sites when compared to the RMSE of MODIS WSA and BSA data (Figure 7). The best performance for the MODIS WSA, BSA, and our retrievals was achieved at the Dali station, with RMSE values of 0.0585, 0.0640, and 0.0422, respectively. At the MAWORS site, the RMSE values for our retrievals were 34% and 31% lower than for WSA

and BSA, respectively (Figure 7). Our algorithm includes the calculation of the effect of terrain on at-surface irradiance and at-surface upwelling radiance and also retrievals albedo for all sky conditions. The average cloud coverage in 2018 at the four stations Dali, NAWORS, MAWORS, and QOMS was 53.9%, 55.7%, 61.0%, and 38.3%, respectively. The four error metrics (Table 3) provide further evidence on the satisfactory performance of our proposed method. The terrain slopes at the four stations—Dali, NAWORS, MAWORS, and QOMS—are 3°, 3°, 5°, and 7°, respectively. It should be noted that our estimates of albedo apply to a plane facet parallel to a 1 km × 1 km terrain facet. The retrievals of surface albedo are based on the mean slope and aspect of the terrain within each 1 km × 1 km grid, determined by averaging slope and aspect calculated at a 30 m × 30 m spatial resolution within each grid. If this facet has the same orientation as the terrain at the location of the radiometer used to measure radiance value, the terrain geometry of our retrievals and in situ measurements should be comparable. The footprint of an in situ radiometer, however, is much smaller than the 1 km × 1 km pixel applied in our retrieval. Differences in aspect have an impact when differences in slope are larger, as it is the case at MAWORS (Table 1), which may explain the lower accuracy of our retrievals at this site. In addition, we noted a few instances of less reliable in situ radiometric measurements, which led to a few outliers with an impact on error metrics difficult to evaluate. The MAWORS site has the highest cloud cover in 2018, with the slope being the second-largest of the four sites. Therefore, it seems to have the greatest atmospheric and topographical influence.

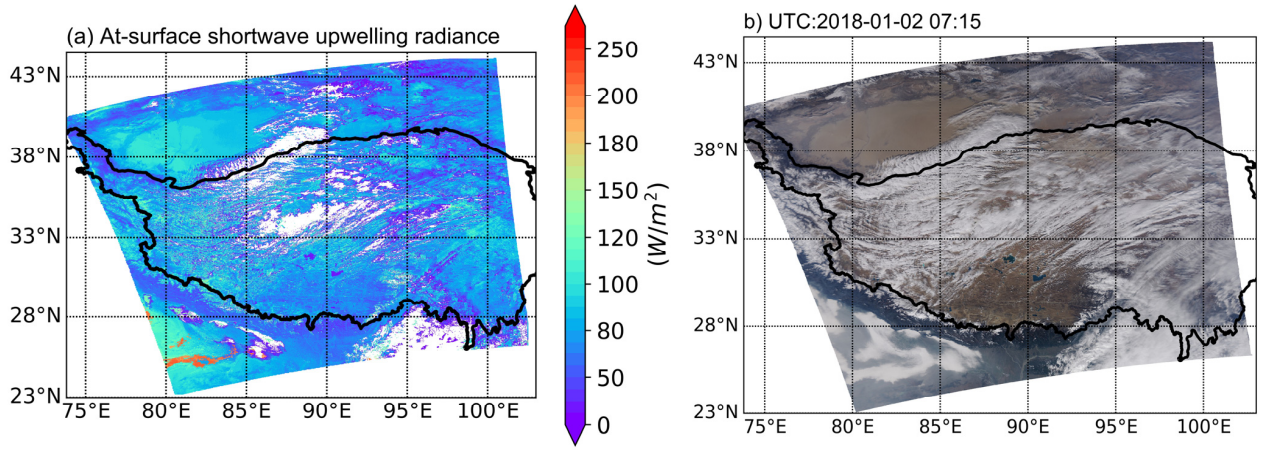

Figure 6. (**a**) The estimates of instantaneous at-surface upwelling radiance of the Tibetan Plateau (MYD Swath: UTC 2018-01-02-0715) and (**b**) MODIS true color composite images of bands 4, 3, and 1 at the same time.

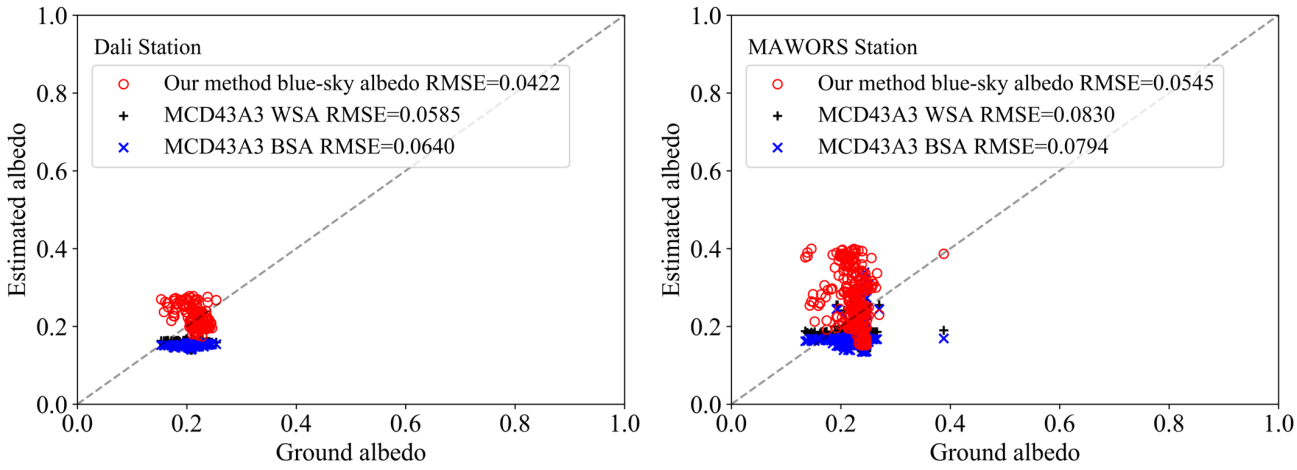

Figure 7. *Cont.*

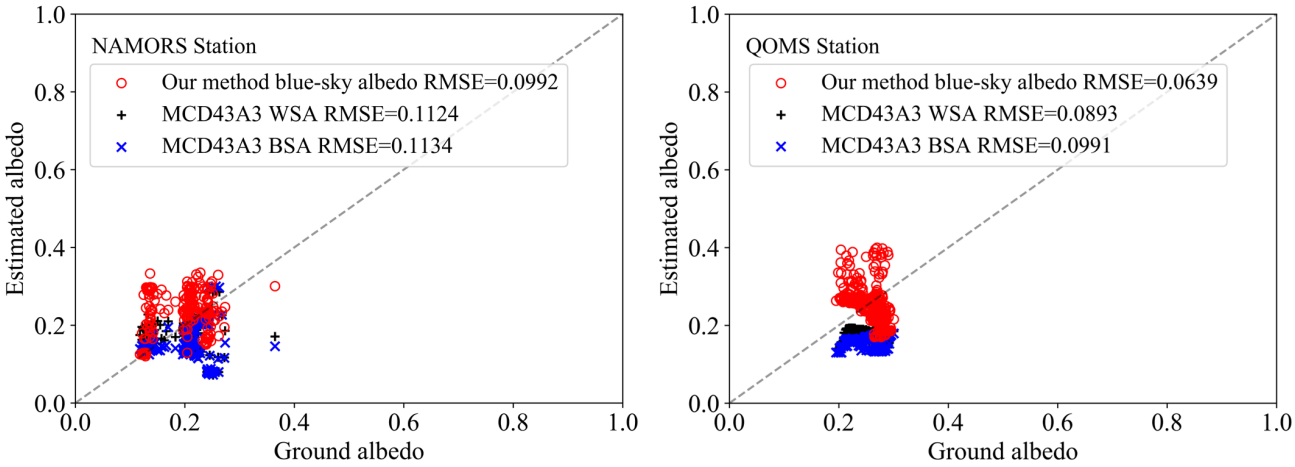

Figure 7. Comparison of clear day results of the estimated broadband surface albedo using the new method proposed in this paper, the MODIS shortwave WSA and BSA and the ground measured albedo at Dali, MAWORS, NAMORS, and QOMS stations on the Tibetan Plateau in 2018.

Table 3. Validation metrics of the estimated surface albedo and comparison with MODIS WSA and BSA under clear sky conditions.

Station	Method	R	RMSE	Bias	MAPE
Dali	Our method	0.44	0.0422	−0.0109	16%
	MODIS WSA	0.30	0.0585	0.054	25%
	MODIS BSA	0.31	0.0640	0.061	28%
NAMORS	Our method	0.26	0.0992	−0.036	20%
	MODIS WSA	0.21	0.1124	0.040	24%
	MODIS BSA	0.20	0.1134	0.043	22%
MAWORS	Our method	0.20	0.0545	−0.035	25%
	MODIS WSA	0.16	0.0830	0.041	23%
	MODIS BSA	0.14	0.0794	0.049	25%
QOMS	Our method	0.42	0.0639	0.012	20%
	MODIS WSA	0.16	0.0893	0.083	31%
	MODIS BSA	0.21	0.0991	0.095	36%

Figure 8 shows the performance of the surface broadband albedo retrievals using our method when compared with ground measurements under different cloud conditions. As expected, the performance was best when the cloud fraction was 0% at Dali, MAWORS, NAMORS, and QOMS. As the cloud fraction increased, the MAPE between the estimated and observed surface albedo increased slightly, i.e., the uncertainty of the estimates increased at Dali and NAWORS but not MAWORS and QOMS (Figure 8).

4.4. Spatial and Temporal Coverage of Retrieved Surface Albedo in Rugged Terrain

Our method improves significantly the spatial and temporal coverage of valid retrievals. The case of the MAWORS station, located in rugged terrain, documents this aspect effectively (Figure 9). Our estimates of surface albedo achieve nearly full spatial coverage (Figure 9f) and, in the cloud-covered areas, show texture characteristics consistent with the surrounding terrain. The high-surface-albedo regions in the MCD43A3 products and our retrievals appear to correlate with flatter areas. By examining areas of mismatch between our results and MCD43A3 albedos, we noted that topography influences surface albedo retrieval, where terrain features like ridges and valleys can cause significant variability (Figure 9). Such terrain effect under cloudy conditions can be captured well by our method, but retrieval with the MODIS albedo products failed (Figure 9d,e). The temporal coverage is also clearly improved by our method, as shown by a time series of the estimated

broadband shortwave surface albedo by our method, the MODIS WSA and BSA, and the ground-measured albedo throughout the year 2018 at MAWORS Station (Figure 10). Gaps in MODIS retrievals from late January to early March were substantial (Figure 10), while there are very few gaps in our retrievals. Moreover, the retrievals on cloudy days (as shown by the gaps in the MODIS albedo time series) are consistent with retrievals on clear-sky days, notwithstanding the larger error in albedo retrieval on cloudy days.

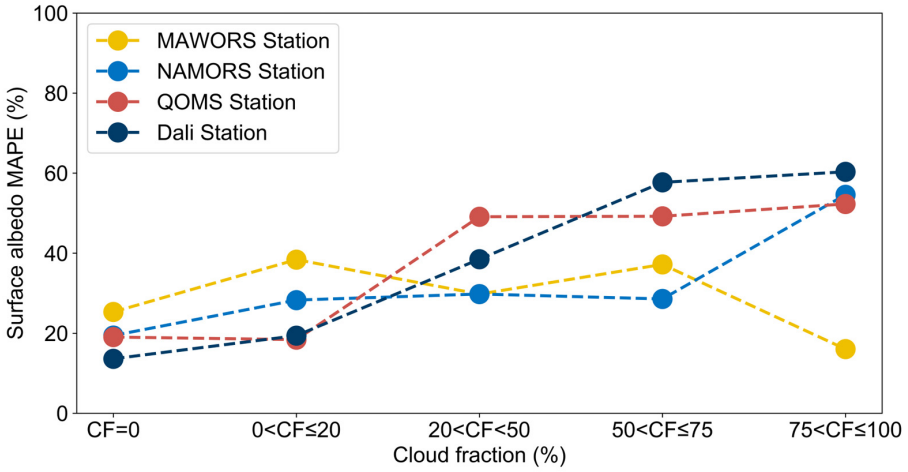

Figure 8. The MAPE between the estimated surface albedo by our method and the ground measurements of albedo at different cloud fractions at Dali, MAWORS, NAMORS, and QOMS stations in 2018.

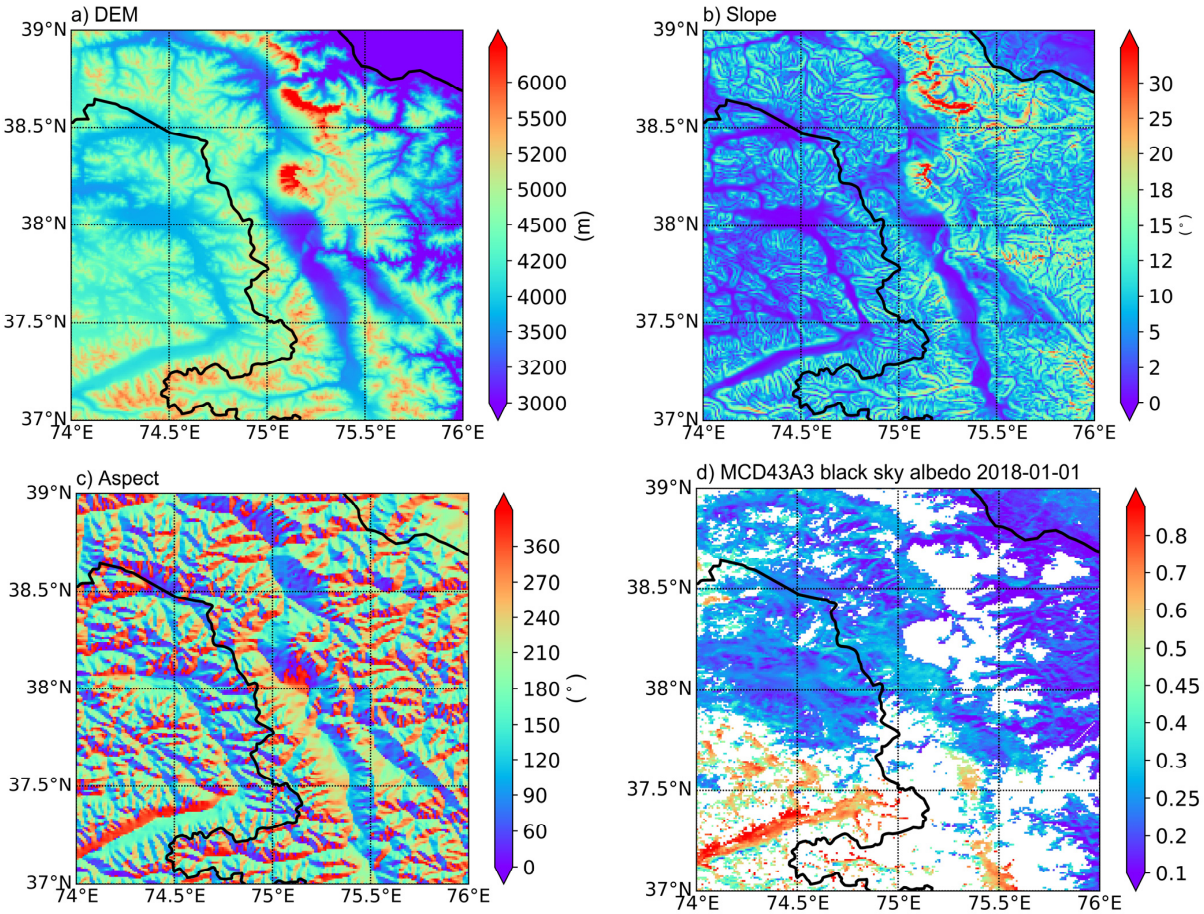

Figure 9. *Cont.*

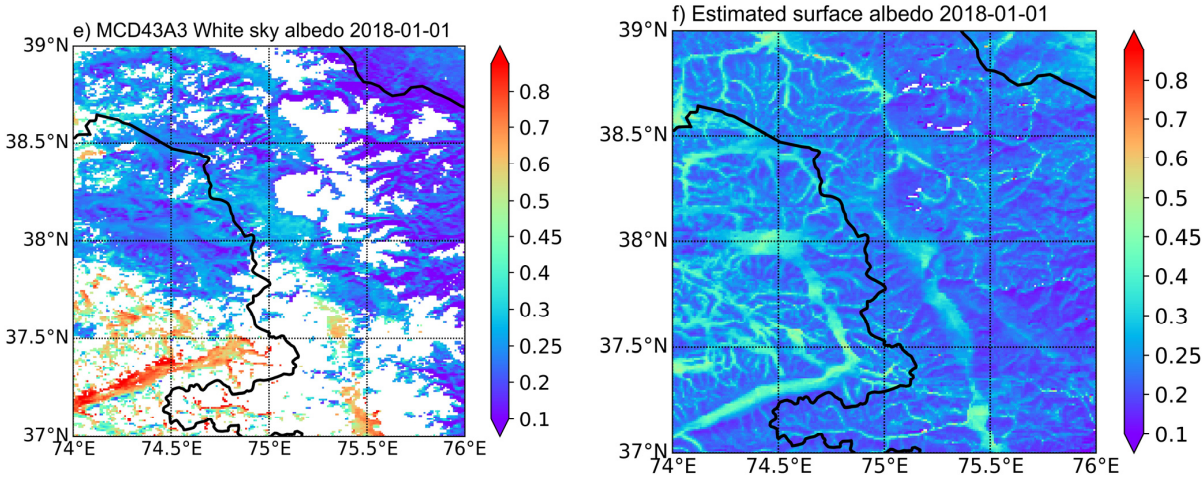

Figure 9. Spatial distribution over an area in the surrounding of the MAWORS station on the Tibetan Plateau: (**a**) elevation (m), (**b**) slope (°), (**c**) aspect (°), (**d**) MCD43A3 black-sky albedo, (**e**) MCD43A3 white-sky albedo, and (**f**) our retrievals of surface broadband albedo on 2018.01.01.

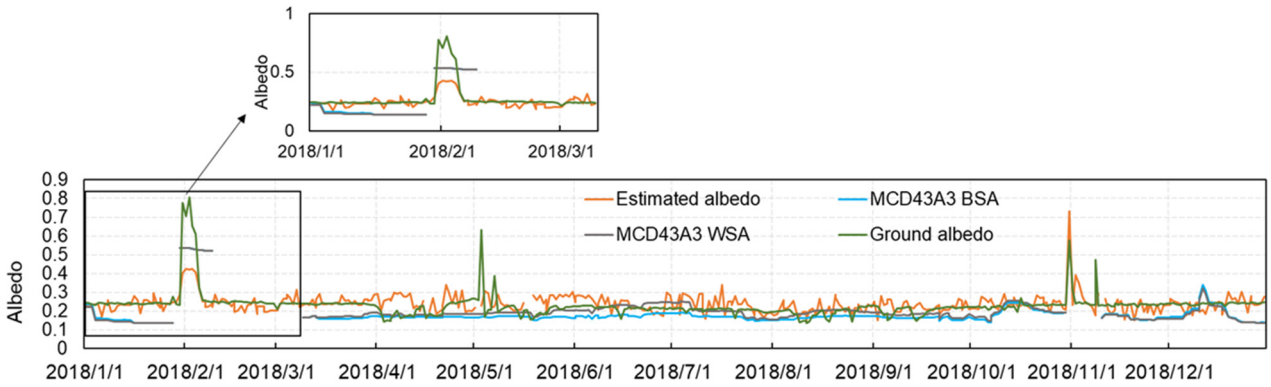

Figure 10. The time series of the estimated broadband surface albedo by our method, MODIS shortwave WSA and BSA, and ground-measured albedo at the MAWORS site on the Tibetan Plateau in 2018.

5. Discussion

5.1. Overall Evaluation of Results

Estimating the surface albedo is of great importance for the regional-scale surface radiation budget and the global climate monitoring of the land–surface–atmosphere system. Moderate-solution satellite data such as MODIS are valuable to generate global daily time series of albedo data products [10]. The limitation in the retrieval of surface albedo relates to a combination of limited available observations to evaluate and improve the retrieval accuracy and the heterogeneity of the land surface.

There are three key issues that warrant further attention. First, this estimation of broadband albedo from a set of narrowband reflectance with conversion coefficients does not necessarily comply with the definition of surface albedo as the ratio of hemispheric radiative fluxes [44,64,65]. This deviation arises because surface albedo, as implied by its definition, has a nonlinear relationship with the incident and reflected narrowband radiance. Moreover, the conversion coefficient set is sensor-specific and cannot be applied universally. Second, the interaction of atmospheric and terrain effects is often oversimplified in the process of estimating surface reflectance from at-satellite radiance at top of atmosphere (TOA) or when estimations are limited to clear sky conditions [66–69]. In reality, optical properties of clouds and aerosols and terrain effects jointly influence the solar radiation reaching the surface. Radiative transfer models that consider the coupled interactions between the rugged terrain and the atmosphere are helpful to improve the quality of

both the derived surface properties (e.g., surface reflectance and albedo) and atmospheric properties (e.g., aerosol loading and size distribution) [70,71] Third, most available albedo products generated through this procedure also assume a flat and homogeneous land surface, as seen in products generated with the data acquired by sensors like MODIS, the multi-angle imaging spectroradiometer (MISR), and polarization and directionality of the earth reflectances (POLDER) [10,72,73].

In this study, we developed a method for estimating instantaneous at-surface shortwave upwelling radiance and surface shortwave albedo under all sky conditions, taking into account the complex interactions between topography and atmosphere on the Tibetan Plateau. This method aimed to reduce the occurrence of data gaps (e.g., due to clouds) and improve the quality of the estimated albedo. Our retrieval method considers all components of all-sky SSI, i.e., direct, isotropic diffuse, circumsolar diffuse, and irradiance from surrounding terrain. This method rests on retrieving at-surface upwelling radiance under all sky conditions to estimate BRF then using the RTLSR model to retrieve daily surface albedo on the Tibetan Plateau at 1 km resolution.

The results show, as expected, that the accuracy of estimated instantaneous at-surface upwelling radiance improves as the cloud fraction decreases, as illustrated in Figure 5. The results also show that the method not only largely reduces the frequency of gaps encountered during albedo retrieval but also improves the surface shortwave albedo retrieval accuracy under clear sky conditions. As expected, the number of valid observations with our method was higher than that with the MCD43A2 product data at four stations on the Tibetan Plateau (Figure 3). Although the R value of at-surface upwelling radiance at Dali Station is relatively low, the model demonstrates small bias and a low RMSE (Figure 4). This station is located in the southeastern Tibetan Plateau, i.e., within the transition region between the Indian and East Asian summer monsoon circulations [74]. The Dali station belongs to a frequently cloudy area, and the percentage of missing observations in the MCD43A3 albedo data is up to 39%. The main reason for low R can be that the temporal resolution of the ground observations is too coarse for the instantaneous at-surface upwelling retrievals at Dali station, where the temporal variability of clouds is very high.

The overall accuracy of estimating surface albedo also improves as the cloud cover decreases (Figure 3). The study highlights that the proposed method for shortwave surface albedo retrieval achieves a substantial increase in the number of valid observations compared to the MODIS MCD43 product. This increase, reaching up to 200% at certain locations, is due to the capability of the new method to estimate the at-surface upwelling radiance under continuous non-clear sky conditions. Our method also improved significantly the spatial and temporal coverage of retrievals, with a high level of consistency between retrievals under cloudy and cloud-free conditions (Figures 9 and 10).

The study also demonstrates that the MCD43A3 albedo model tends to underestimate surface shortwave albedo when compared with ground measurements at four stations on the Tibetan Plateau (alpine steppe and farmland) over sparsely vegetated areas, consistent with the literature [75–77]. Using the increased number of valid observations under all sky conditions and taking topography effect into account, our method shows a significant improvement in RMSE values at the observation sites compared to the MCD43A3 data, indicating a more accurate reflection of terrain and atmospheric influences on albedo.

5.2. Limitations of Our Method

Distinguishing between snow/ice and cloud cover in multispectral imagery can be challenging due to their similar spectral properties [78]. Clouds typically exhibit higher reflectance in the visible (VIS), near-infrared (NIR), and shortwave infrared (SWIR) bands along with lower temperatures compared to the underlying Earth surface. Cloud detection relies on well-defined characteristics, such as high reflectance in VIS and NIR/SWIR bands, coupled with lower temperatures in thermal bands. Establishing accurate reflectance and temperature thresholds facilitates the identification of diverse cloud types. Resolving spatial heterogeneity of snowfall over the Tibetan Plateau is a challenge, impacting the accuracy

of retrieved albedo. The misclassification of snow as clouds in the MOD06/MYD06 cloud data product leads to inaccuracies in the retrieved albedo. The snow-covered surfaces have high albedo, and mistaking these areas for clouds can result in inaccurate estimations of the surface albedo.

In our calculation of at-surface upwelling radiance and surface albedo under cloudy conditions, we assume that the cloud distribution within a pixel is uniform, plane-parallel, and static. However, the validity of this assumption depends on the specific type of cloud and its actual spatial distribution within the pixel, which can result in significant discrepancies between our estimates and observations. In Stephens's model [30] used in this study, it is assumed that the clouds are liquid water clouds, and assuming the wrong cloud type can lead to less accurate estimates of cloud reflectance and transmittance.

Terrain has multiple impacts on albedo across spatial scales [16]. Hao et al. [20] focused on a quantitative exploration of the topographic effect, elucidating that the BSA exhibits a decreasing trend with an increase in mean slope. Moreover, an augmented solar zenith angle accentuates the diminishing trend in BSA, particularly as mean terrain slope increases. Gao et al. [21] proposed an improved method by removing the surrounding topographic effect on land surface reflectance and considering the topographic effect in retrieving land surface albedo. By considering the influence of the topography, our method incorporates various critical factors such as the illumination angle, observing angle, effects of shadowing, and the reflectance of radiation due to the surrounding terrain. Currently, we can retrieve surface albedo with a spatial resolution of 1 km $\times$ 1 km. However, this resolution restricts our ability to accurately capture the heterogeneity of land cover within each 1 km $\times$ 1 km pixel. Such pixels may contain diverse land cover types, each with distinct albedo properties, and this diversity can result in a generalized smoothing effect that conceals minor variations. Our method may still be inadequate to reveal complex terrain and land cover changes at the sub-pixel level. Wen et al. [79] illustrated the scaling effects and the necessary corrections for surface albedo assessments in rugged terrain, while Liu et al. [80] have provided insights into how sub-pixel details can refine our understanding of pixel-wide land surface albedo. Furthermore, Wen et al. [81] has introduced an advanced multi-sensor BRDF inversion model, designed specifically to account for sub-pixel topographic influences. These studies collectively underscore the value of integrating sub-pixel topography and land cover data to enhance the accuracy of surface BRDF and land surface albedo estimations, particularly in rugged terrain. Future advancements could stem from accounting for the spatial variability of terrain at the sub-pixel level, utilizing high-resolution DEM data and sophisticated downscaling methods. Such refinements are anticipated to bridge the gap between current capabilities and the nuanced realities of terrain effects on albedo measurements.

The tower-mounted radiometers used to measure radiative fluxes at the land-atmosphere interface are typically installed horizontally on flat terrain, i.e., the field-measured shortwave upward and downward radiation apply to a flat and horizontal plane. These conditions apply to the radiometers installed at our four stations (i.e., QOMS, MAWORS, NAMORS and Dali; see Table 1), where the slopes are about 5° or less (Table 1). On the other hand, our estimates of shortwave upward and downward radiation apply to the plane parallel to a 1 km $\times$ 1 km terrain facet. This means that the footprints captured by space-borne and in situ radiometers may be inherently different. Radiometers on the ground are usually designed to measure all-sky radiation from all directions.

In situ radiometers observe at-surface upwelling radiance from an entire hemisphere, but mostly originating from a small area on the surface, and atmospheric conditions have limited impact. However, satellite observations are more influenced by atmospheric conditions, as they record radiation from a larger area and are impacted by highly variable atmospheric factors, such as cloud cover and atmospheric aerosols. The accuracy of estimating at-surface upwelling radiance using satellite data is more complicated due to the limitations of satellite observation angles and distance. This makes it more difficult to match in situ measurements of at-surface upwelling radiance. The study estimated

at-surface upwelling radiance and surface albedo by averaging the slope and aspect of the terrain within each 1 km × 1 km grid, calculated from 30 m × 30 m resolution data. This approach ensures that the terrain orientation in the retrieval process aligns with that at the radiometer location, providing comparable terrain geometry apply. However, the radiometer's footprint is significantly smaller than the 1 km × 1 km pixel used in the retrieval.

In summary, our method has made certain advancements in estimating all-sky surface albedo over rugged terrain on the Tibetan Plateau, but it also reveals several potential limitations and directions for improvement. Future research should focus on enhancing the model adaptability to complex terrains and varying climatic conditions, further improving estimation accuracy and reliability. Through continuous validation, calibration, and refinement, we anticipate further enhancing our understanding and representation of the complex interplay between surface characteristics and atmospheric conditions on the Tibetan Plateau.

6. Conclusions

The primary aim of this study was to introduce an innovative approach for the all-sky retrieval of surface albedo across the Tibetan Plateau with consideration of the terrain characteristics and atmospheric effects, particularly clouds. This method was designed to significantly reduce the occurrence of data gaps mainly due to clouds and enhance the accuracy of the estimated albedo. Notably, in a previous companion study, we addressed the retrieval of surface solar irradiance and its four components, including direct, isotropic diffuse, circumsolar diffuse, and surrounding terrain irradiance. Both surface solar irradiance and at-surface upwelling radiance have been estimated by accounting for the actual terrain geometry derived from DEM data. Under cloudy conditions, the radiative transfer model incorporates cloud properties such as cloud cover fraction, reflectance, and transmittance to estimate surface solar irradiance and at-surface upwelling radiance. The RTLSR kernel-driven model is utilized to describe the BRDF of observed targets and to estimate the reflectance for the four components of SSI in all sky conditions, which are subsequently used to determine the total reflected irradiance within the viewing hemisphere. Ultimately, the surface albedo is calculated as the ratio of the total reflected radiance to the total incident solar irradiance, in alignment with the fundamental concept of surface albedo.

Our study demonstrates that by integrating terrain information and cloud properties into radiative transfer modeling, the accuracy of estimating surface albedo and radiance in complex terrains can be effectively improved. This method is significant for understanding and monitoring the surface radiation energy balance in complex terrain areas like the Tibetan Plateau and provides more accurate input data for climate modeling and analysis. We anticipate that the outcomes of our research will offer a viable solution for accurate estimation of surface albedo on a global scale and will have a positive impact on global change research and environmental monitoring.

Author Contributions: Conceptualization, J.J., M.M. and L.J.; methodology, J.J., M.M. and L.J.; software, J.J.; validation, J.J.; formal analysis, J.J., M.M., L.J. and Q.C.; investigation, J.J., M.M. and L.J.; resources, L.J. and M.M.; data curation, J.J., L.J. and A.X.; writing—original draft preparation, J.J.; writing—review and editing, L.J., M.M. and Q.C.; visualization, J.J.; supervision, M.M. and L.J.; project administration, L.J. and M.M.; funding acquisition, L.J. and M.M. All authors have read and agreed to the published version of the manuscript.

Funding: This research was jointly funded by the Second Tibetan Plateau Scientific Expedition and Research Program (STEP) (Grant No. 2019QZKK0103) and the National Natural Science Foundation of China project (Grant No. 91737205). MM acknowledges the support of the Chinese Academy of Sciences President's International Fellowship Initiative (Grant No. 2020VTA0001) and the MOST High Level Foreign Expert Program (Grant No. G2022055010L).

Data Availability Statement: The datasets presented in this article are not readily available because the data are part of an ongoing study.

Acknowledgments: We thank the Institute of Tibetan Plateau Research of the Chinese Academy of Sciences and the Dali National Climate Observatory for providing valuable ground observation data.

Conflicts of Interest: The authors declare no conflicts of interest.

References

1. Zhang, X.; Jiao, Z.; Zhao, C.; Qu, Y.; Liu, Q.; Zhang, H.; Tong, Y.; Wang, C.; Li, S.; Guo, J.; et al. Review of Land Surface Albedo: Variance Characteristics, Climate Effect and Management Strategy. *Remote Sens.* **2022**, *14*, 1382. [CrossRef]
2. Dickinson, R.E. Land Surface Processes and Climate—Surface Albedos and Energy Balance. In *Theory of Climate, Proceedings of a Symposium Commemorating the Two-Hundredth Anniversary of the Academy of Sciences of Lisbon*; Saltzman, B., Ed.; Advances in Geophysics; Elsevier: Amsterdam, The Netherlands, 1983; Volume 25, pp. 305–353.
3. Henderson-Sellers, A.; Wilson, M.F. Surface albedo data for climatic modeling. *Rev. Geophys.* **1983**, *21*, 1743–1778. [CrossRef]
4. Liang, S.; Zhao, X.; Liu, S.; Yuan, W.; Cheng, X.; Xiao, Z.; Zhang, X.; Liu, Q.; Cheng, J.; Tang, H.; et al. A long-term Global LAnd Surface Satellite (GLASS) data-set for environmental studies. *Int. J. Digit. Earth* **2013**, *6*, 5–33. [CrossRef]
5. Dickinson, R.E. Land processes in climate models. *Remote Sens. Environ.* **1995**, *51*, 27–38. [CrossRef]
6. Sellers, P.J.; Meeson, B.W.; Hall, F.G.; Asrar, G.; Murphy, R.E.; Schiffer, R.A.; Bretherton, F.P.; Dickinson, R.E.; Ellingson, R.G.; Field, C.B.; et al. Remote sensing of the land surface for studies of global change: Models—Algorithms—Experiments. *Remote Sens. Environ.* **1995**, *51*, 3–26. [CrossRef]
7. Ma, Y.; Yao, T.; Zhong, L.; Wang, B.; Xu, X.; Hu, Z.; Ma, W.; Sun, F.; Han, C.; Li, M.; et al. Comprehensive study of energy and water exchange over the Tibetan Plateau: A review and perspective: From GAME/Tibet and CAMP/Tibet to TORP, TPEORP, and TPEITORP. *Earth-Sci. Rev.* **2023**, *237*, 104312. [CrossRef]
8. Lin, X.; Wen, J.; Liu, Q.; You, D.; Wu, S.; Hao, D.; Xiao, Q.; Zhang, Z.; Zhang, Z. Spatiotemporal Variability of Land Surface Albedo over the Tibet Plateau from 2001 to 2019. *Remote Sens.* **2020**, *12*, 1188. [CrossRef]
9. Qu, Y.; Liang, S.; Liu, Q.; He, T.; Liu, S.; Li, X. Mapping Surface Broadband Albedo from Satellite Observations: A Review of Literatures on Algorithms and Products. *Remote Sens.* **2015**, *7*, 990–1020. [CrossRef]
10. Schaaf, C.B.; Gao, F.; Strahler, A.H.; Lucht, W.; Li, X.; Tsang, T.; Strugnell, N.C.; Zhang, X.; Jin, Y.; Muller, J.-P.; et al. First operational BRDF, albedo nadir reflectance products from MODIS. *Remote Sens. Environ.* **2002**, *83*, 135–148. [CrossRef]
11. Strahler, A.H.; Muller, J.-P.; MODIS Science Team Members. MODIS BRDF/Albedo Product: Algorithm Theoretical Basis Document Version 5.0. *MODIS Doc.* **1999**, *23*, 42–47.
12. Jin, Y.; Schaaf, C.B.; Gao, F.; Li, X.; Strahler, A.H.; Lucht, W.; Liang, S. Consistency of MODIS surface bidirectional reflectance distribution function and albedo retrievals: 1. Algorithm performance. *J. Geophys. Res. Atmos.* **2003**, *108*. [CrossRef]
13. Aijun, C.; Lingen, B.; Yujie, L. Deriving albedo over cloudy areas with composite inversion. *Proc. SPIE* **2007**, *6753*, 75337.
14. Liu, N.F.; Liu, Q.; Wang, L.Z.; Liang, S.L.; Wen, J.G.; Qu, Y.; Liu, S.H. A statistics-based temporal filter algorithm to map spatiotemporally continuous shortwave albedo from MODIS data. *Hydrol. Earth Syst. Sci.* **2013**, *17*, 2121–2129. [CrossRef]
15. Vermote, E.F.; El Saleous, N.Z.; Justice, C.O. Atmospheric correction of MODIS data in the visible to middle infrared: First results. *Remote Sens. Environ.* **2002**, *83*, 97–111. [CrossRef]
16. Ju, J.; Roy, D.P.; Shuai, Y.; Schaaf, C. Development of an approach for generation of temporally complete daily nadir MODIS reflectance time series. *Remote Sens. Environ.* **2010**, *114*, 1–20. [CrossRef]
17. Samain, O.; Geiger, B.; Roujean, J.L. Spectral Normalization and Fusion of Optical Sensors for the Retrieval of BRDF and Albedo: Application to VEGETATION, MODIS, and MERIS Data Sets. *IEEE Trans. Geosci. Remote Sens.* **2006**, *44*, 3166–3179. [CrossRef]
18. Quaife, T.; Lewis, P. Temporal Constraints on Linear BRDF Model Parameters. *IEEE Trans. Geosci. Remote Sens.* **2010**, *48*, 2445–2450. [CrossRef]
19. Moody, E.G.; King, M.D.; Platnick, S.; Schaaf, C.B.; Feng, G. Spatially complete global spectral surface albedos: Value-added datasets derived from Terra MODIS land products. *IEEE Trans. Geosci. Remote Sens.* **2005**, *43*, 144–158. [CrossRef]
20. Hao, D.; Wen, J.; Xiao, Q.; Wu, S.; Lin, X.; Dou, B.; You, D.; Tang, Y. Simulation and Analysis of the Topographic Effects on Snow-Free Albedo over Rugged Terrain. *Remote Sens.* **2018**, *10*, 278. [CrossRef]
21. Gao, B.; Jia, L.; Menenti, M. An Improved Method for Retrieving Land Surface Albedo Over Rugged Terrain. *IEEE Geosci. Remote Sens. Lett.* **2014**, *11*, 554–558. [CrossRef]
22. Wen, J.; Lin, X.; Wu, X.; Bao, Y.; You, D.; Gong, B.; Tang, Y.; Wu, S.; Xiao, Q.; Liu, Q. Validation of the MCD43A3 Collection 6 and GLASS V04 Snow-Free Albedo Products Over Rugged Terrain. *IEEE Trans. Geosci. Remote Sens.* **2022**, *60*, 1–11. [CrossRef]
23. Yang, C.; Vidal, A. Combination of digital elevation models with SPOT-1 HRV multispectral imagery for reflectance factor mapping. *Remote Sens. Environ.* **1990**, *32*, 35–45. [CrossRef]
24. Roupioz, L.; Nerry, F.; Jia, L.; Menenti, M. Improved Surface Reflectance from Remote Sensing Data with Sub-Pixel Topographic Information. *Remote Sens.* **2014**, *6*, 10356–10374. [CrossRef]
25. Roupioz, L.; Jia, L.; Nerry, F.; Menenti, M. Correction of sub-pixel topographical effects on land surface albedo retrieved from geostationary satellite (FengYun-2D) observations. *IOP Conf. Ser. Earth Environ. Sci.* **2014**, *17*, 012270. [CrossRef]
26. Ma, Y.; Pinker, R.T. Modeling shortwave radiative fluxes from satellites. *J. Geophys. Res. Atmos.* **2012**, *117*. [CrossRef]

27. Pinker, R.T.; Laszlo, I. Modeling Surface Solar Irradiance for Satellite Applications on a Global Scale. *J. Appl. Meteorol. Climatol.* **1992**, *31*, 194–211. [CrossRef]
28. Tang, W.; Qin, J.; Yang, K.; Liu, S.; Lu, N.; Niu, X. Retrieving high-resolution surface solar radiation with cloud parameters derived by combining MODIS and MTSAT data. *Atmos. Chem. Phys.* **2016**, *16*, 2543–2557. [CrossRef]
29. Liang, S.; Zheng, T.; Wang, D.; Wang, K.; Liu, R.; Tsay, S.-C.; Running, S.; Townshend, J. Mapping High-Resolution Incident Photosynthetically Active Radiation over Land from Polar-Orbiting and Geostationary Satellite Data. *Photogramm. Eng. Remote Sens.* **2007**, *73*, 1085–1089.
30. Stephens, G.L.; Ackerman, S.; Smith, E.A. A Shortwave Parameterization Revised to Improve Cloud Absorption. *J. Atmos. Sci.* **1984**, *41*, 687–690. [CrossRef]
31. Slingo, A. A GCM parameterization for the shortwave radiative properties of water clouds. *J. Atmos. Sci.* **1989**, *46*, 1419–1427. [CrossRef]
32. Fu, Q.; Yang, P.; Sun, W.B. An Accurate Parameterization of the Infrared Radiative Properties of Cirrus Clouds for Climate Models. *J. Clim.* **1998**, *11*, 2223–2237. [CrossRef]
33. Van Laake, P.E.; Sanchez-Azofeifa, G.A. Simplified atmospheric radiative transfer modelling for estimating incident PAR using MODIS atmosphere products. *Remote Sens. Environ.* **2004**, *91*, 98–113. [CrossRef]
34. Huang, G.; Liu, S.; Liang, S. Estimation of net surface shortwave radiation from MODIS data. *Int. J. Remote Sens.* **2012**, *33*, 804–825. [CrossRef]
35. Huang, G.; Liang, S.; Lu, N.; Ma, M.; Wang, D. Toward a Broadband Parameterization Scheme for Estimating Surface Solar Irradiance: Development and Preliminary Results on MODIS Products. *J. Geophys. Res. Atmos.* **2018**, *123*, 12,180–12,193. [CrossRef]
36. Cano, D.; Monget, J.M.; Albuisson, M.; Guillard, H.; Regas, N.; Wald, L. A method for the determination of the global solar radiation from meteorological satellite data. *Solar Energy* **1986**, *37*, 31–39. [CrossRef]
37. Hammer, A.; Heinemann, D.; Hoyer, C.; Kuhlemann, R.; Lorenz, E.; Müller, R.; Beyer, H.G. Solar energy assessment using remote sensing technologies. *Remote Sens. Environ.* **2003**, *86*, 423–432. [CrossRef]
38. Zhang, Y.; He, T.; Liang, S.; Wang, D.; Yu, Y. Estimation of all-sky instantaneous surface incident shortwave radiation from Moderate Resolution Imaging Spectroradiometer data using optimization method. *Remote Sens. Environ.* **2018**, *209*, 468–479. [CrossRef]
39. Wang, T.; Yan, G.; Chen, L. Consistent retrieval methods to estimate land surface shortwave and longwave radiative flux components under clear-sky conditions. *Remote Sens. Environ.* **2012**, *124*, 61–71. [CrossRef]
40. Ryu, Y.; Jiang, C.; Kobayashi, H.; Detto, M. MODIS-derived global land products of shortwave radiation and diffuse and total photosynthetically active radiation at 5 km resolution from 2000. *Remote Sens. Environ.* **2018**, *204*, 812–825. [CrossRef]
41. Yang, L.; Zhang, X.; Liang, S.; Yao, Y.; Jia, K.; Jia, A. Estimating Surface Downward Shortwave Radiation over China Based on the Gradient Boosting Decision Tree Method. *Remote Sens.* **2018**, *10*, 185. [CrossRef]
42. Jia, J.; Menenti, M.; Jia, L.; Chen, Q.; Xu, A. Estimation of All-Sky Solar Irradiance Components over Rugged Terrain Using Satellite and Reanalysis Data: The Tibetan Plateau Experiment. *IEEE Trans. Geosci. Remote Sens.* **2024**.
43. Zhu, C.-S.; Cao, J.-J.; Xu, B.; Huang, R.-J.; Wang, P.; Ho, K.F.; Shen, Z.; Liu, S.-X.; Han, Y.; Tie, X.-X.; et al. Black Carbon Aerosols at Mt. Muztagh Ata, a High-Altitude Location in the Western Tibetan Plateau. *Aerosol Air Qual. Res.* **2016**, *16*, 752–763. [CrossRef]
44. Peng, S.; Wen, J.; Xiao, Q.; You, D.; Dou, B.; Liu, Q.; Tang, Y. Multi-Staged NDVI Dependent Snow-Free Land-Surface Shortwave Albedo Narrowband-to-Broadband (NTB) Coefficients and Their Sensitivity Analysis. *Remote Sens.* **2017**, *9*, 93. [CrossRef]
45. Ma, Y.; Hu, Z.; Xie, Z.; Ma, W.; Wang, B.; Chen, X.; Li, M.; Zhong, L.; Sun, F.; Gu, L.; et al. A long-term (2005–2016) dataset of hourly integrated land–atmosphere interaction observations on the Tibetan Plateau. Earth Syst. *Sci. Data* **2020**, *12*, 2937–2957. [CrossRef]
46. Liu, H.; Feng, J.; Sun, J.; Wang, L.; Xu, A. Eddy covariance measurements of water vapor and CO_2 fluxes above the Erhai Lake. *Sci. China Earth Sci.* **2015**, *58*, 317–328. [CrossRef]
47. Tang, B.; Li, Z.-L.; Zhang, R. A direct method for estimating net surface shortwave radiation from MODIS data. *Remote Sens. Environ.* **2006**, *103*, 115–126. [CrossRef]
48. Zaksek, K.; Oštir, K.; Kokalj, Ž. Sky-View Factor as a Relief Visualization Technique. *Remote Sens.* **2011**, *3*, 398. [CrossRef]
49. Allen, R.G.; Trezza, R.; Tasumi, M. Analytical integrated functions for daily solar radiation on slopes. *Agric. For. Meteorol.* **2006**, *139*, 55–73. [CrossRef]
50. Sandmeier, S.; Itten, K.I. A physically-based model to correct atmospheric and illumination effects in optical satellite data of rugged terrain. *IEEE Trans. Geosci. Remote Sens.* **1997**, *35*, 708–717. [CrossRef]
51. Dubayah, R. Estimating net solar radiation using Landsat Thematic Mapper and digital elevation data. *Water Resour. Res.* **1992**, *28*, 2469–2484. [CrossRef]
52. Lucht, W.; Schaaf, C.B.; Strahler, A.H. An algorithm for the retrieval of albedo from space using semiempirical BRDF models. *IEEE Trans. Geosci. Remote Sens.* **2000**, *38*, 977–998. [CrossRef]
53. Yang, K.; Huang, G.W.; Tamai, N. A hybrid model for estimating global solar radiation. *Sol. Energy* **2001**, *70*, 13–22. [CrossRef]
54. Duguay, C.R. An approach to the estimation of surface net radiation in mountain areas using remote sensing and digital terrain data. *Theor. Appl. Climatol.* **1995**, *52*, 55–68. [CrossRef]

55. Dozier, J.; Bruno, J.; Downey, P. Faster solution to the horizon problem. *Comput. Geosci.* **1981**, *7*, 145–151. [CrossRef]
56. Hay, J.E. Calculation of monthly mean solar radiation for horizontal and inclined surfaces. *Sol. Energy* **1979**, *23*, 301–307. [CrossRef]
57. Yang, K.; Koike, T.; Huang, G.; Tamai, N.J.R.d.i.s.e. Development and validation of an advanced model for estimating solar radiation from surface meteorological data. *Recent Dev. Sol. Energy* **2007**, *1*, 53.
58. Stephens, G.L. Radiation Profiles in Extended Water Clouds. II: Parameterization Schemes. *J. Atmos. Sci.* **1978**, *35*, 2123–2132. [CrossRef]
59. Lin, X.; Wu, S.; Hao, D.; Wen, J.; Xiao, Q.; Liu, Q. Sloping Surface Reflectance: The Best Option for Satellite-Based Albedo Retrieval Over Mountainous Areas. *IEEE Geosci. Remote Sens. Lett.* **2021**, *19*, 3002705. [CrossRef]
60. Schaepman-Strub, G.; Schaepman, M.E.; Painter, T.H.; Dangel, S.; Martonchik, J.V. Reflectance quantities in optical remote sensing—Definitions and case studies. *Remote Sens. Environ.* **2006**, *103*, 27–42. [CrossRef]
61. Huang, X.; Jiao, Z.; Dong, Y.; Zhang, H.; Li, X. Analysis of BRDF and Albedo Retrieved by Kernel-Driven Models Using Field Measurements. *IEEE J. Sel. Top. Appl. Earth Obs. Remote Sens.* **2013**, *6*, 149–161. [CrossRef]
62. Wanner, W.; Li, X.; Strahler, A.H. On the derivation of kernels for kernel-driven models of bidirectional reflectance. *J. Geophys. Res. Atmos.* **1995**, *100*, 21077–21089. [CrossRef]
63. Chrysoulakis, N.; Mitraka, Z.; Gorelick, N. Exploiting satellite observations for global surface albedo trends monitoring. *Theor. Appl. Climatol.* **2019**, *137*, 1171–1179. [CrossRef]
64. Liang, S. Narrowband to broadband conversions of land surface albedo I: Algorithms. *Remote Sens. Environ.* **2001**, *76*, 213–238. [CrossRef]
65. Carrer, D.; Pinault, F.; Lellouch, G.; Trigo, I.F.; Benhadj, I.; Camacho, F.; Ceamanos, X.; Moparthy, S.; Munoz-Sabater, J.; Schüller, L.; et al. Surface Albedo Retrieval from 40-Years of Earth Observations through the EUMETSAT/LSA SAF and EU/C3S Programmes: The Versatile Algorithm of PYALUS. *Remote Sens.* **2021**, *13*, 372. [CrossRef]
66. Chavez, P.S. An improved dark-object subtraction technique for atmospheric scattering correction of multispectral data. *Remote Sens. Environ.* **1988**, *24*, 459–479. [CrossRef]
67. Smith, G.M.; Milton, E.J. The use of the empirical line method to calibrate remotely sensed data to reflectance. *Int. J. Remote Sens.* **1999**, *20*, 2653–2662. [CrossRef]
68. Nazeer, M.; Nichol, J.E.; Yung, Y.-K. Evaluation of atmospheric correction models and Landsat surface reflectance product in an urban coastal environment. *Int. J. Remote Sens.* **2014**, *35*, 6271–6291. [CrossRef]
69. Bilal, M.; Nazeer, M.; Nichol, J.E.; Bleiweiss, M.P.; Qiu, Z.; Jäkel, E.; Campbell, J.R.; Atique, L.; Huang, X.; Lolli, S. A Simplified and Robust Surface Reflectance Estimation Method (SREM) for Use over Diverse Land Surfaces Using Multi-Sensor Data. *Remote Sens.* **2019**, *11*, 1344. [CrossRef]
70. Govaerts, Y.M.; Wagner, S.; Lattanzio, A.; Watts, P. Joint retrieval of surface reflectance and aerosol optical depth from MSG/SEVIRI observations with an optimal estimation approach: 1. Theory. *J. Geophys. Res. Atmos.* **2010**, *115*. [CrossRef]
71. Shi, H.; Xiao, Z.; Wen, J.; Wu, S. An Optical–Thermal Surface–Atmosphere Radiative Transfer Model Coupling Framework With Topographic Effects. *IEEE Trans. Geosci. Remote Sens.* **2022**, *60*, 4400312. [CrossRef]
72. Deschamps, P.; Breon, F.-M.; Leroy, M.; Podaire, A.; Bricaud, A.; Buriez, J.C.; Seze, G. The POLDER Mission: Instrument Characteristics and Scientific Objectives. *IEEE Trans. Geosci. Remote Sens.* **1994**, *32*, 598–615. [CrossRef]
73. Diner, D.J.; Beckert, J.C.; Reilly, T.H.; Bruegge, C.J.; Conel, J.E.; Kahn, R.A.; Martonchik, J.V.; Ackerman, T.P.; Davies, R.; Gerstl, S.A.W.; et al. Multi-angle Imaging SpectroRadiometer (MISR) instrument description and experiment overview. *IEEE Trans. Geosci. Remote Sens.* **1998**, *36*, 1072–1087. [CrossRef]
74. Shi, Z.; Sha, Y.; Liu, X. Effect of Yunnan–Guizhou Topography at the Southeastern Tibetan Plateau on the Indian Monsoon. *J. Clim.* **2017**, *30*, 1259–1272. [CrossRef]
75. Sobrino, J.A.; Franch, B.; Oltra-Carrió, R.; Vermote, E.F.; Fedele, E. Evaluation of the MODIS Albedo product over a heterogeneous agricultural area. *Int. J. Remote Sens.* **2013**, *34*, 5530–5540. [CrossRef]
76. Cescatti, A.; Marcolla, B.; Santhana Vannan, S.K.; Pan, J.Y.; Román, M.O.; Yang, X.; Ciais, P.; Cook, R.B.; Law, B.E.; Matteucci, G.; et al. Intercomparison of MODIS albedo retrievals and in situ measurements across the global FLUXNET network. *Remote Sens. Environ.* **2012**, *121*, 323–334. [CrossRef]
77. Zhang, H.; Zhang, X.; Cui, L.; Dong, Y.; Liu, Y.; Xi, Q.; Cao, H.; Chen, L.; Lian, Y. Enhancing Leaf Area Index Estimation with MODIS BRDF Data by Optimizing Directional Observations and Integrating PROSAIL and Ross–Li Models. *Remote Sens.* **2023**, *15*, 5609. [CrossRef]
78. Stillinger, T.; Roberts, D.A.; Collar, N.M.; Dozier, J. Cloud Masking for Landsat 8 and MODIS Terra Over Snow-Covered Terrain: Error Analysis and Spectral Similarity between Snow and Cloud. *Water Resour. Res.* **2019**, *55*, 6169–6184. [CrossRef] [PubMed]
79. Wen, J.; Liu, Q.; Liu, Q.; Xiao, Q.; Li, X. Scale effect and scale correction of land-surface albedo in rugged terrain. *Int. J. Remote Sens.* **2009**, *30*, 5397–5420. [CrossRef]

80. Liu, W.; Hu, B.; Wang, S. Improving Land Surface Pixel Level Albedo Characterization Using Sub-Pixel Information Retrieved from Remote Sensing. In Proceedings of the IGARSS 2008—2008 IEEE International Geoscience and Remote Sensing Symposium, Boston, MA, USA, 7–11 July 2008; Volume 2, pp. 801–804.
81. Wen, J.; You, D.; Han, Y.; Lin, X.; Wu, S.; Tang, Y.; Xiao, Q.; Liu, Q. Estimating Surface BRDF/Albedo over Rugged Terrain Using an Extended Multi-Sensor Combined BRDF Inversion (EMCBI) Model. *IEEE Geosci. Remote Sens. Lett.* **2022**, *19*, 2503505. [CrossRef]